atmosphere

MDPI

Article

Coupling Large Eddies and Waves in Turbulence: Case Study of Magnetic Helicity at the Ion Inertial Scale

Annick Pouquet [1,2,†,*], Julia E. Stawarz [3,†] and Duane Rosenberg [4]

[1] Laboratory for Atmospheric and Space Physics, University of Colorado, Boulder, CO 80309, USA
[2] National Center for Atmospheric Research, P.O. Box 3000, Boulder, CO 80307, USA
[3] Department of Physics, Imperial College London, London SW7 2BU, UK; j.stawarz@imperial.ac.uk
[4] 288 Harper St., Louisville, CO 80027, USA; duaner62@gmail.com
* Correspondence: pouquet@ucar.edu
† Both authors contributed equally to this work.

Received: 5 January 2020; Accepted: 1 February 2020; Published: 14 February 2020

Abstract: In turbulence, for neutral or conducting fluids, a large ratio of scales is excited because of the possible occurrence of inverse cascades to large, global scales together with direct cascades to small, dissipative scales, as observed in the atmosphere and oceans, or in the solar environment. In this context, using direct numerical simulations with forcing, we analyze scale dynamics in the presence of magnetic fields with a generalized Ohm's law including a Hall current. The ion inertial length ϵ_H serves as the control parameter at fixed Reynolds number. Both the magnetic and generalized helicity—invariants in the ideal case—grow linearly with time, as expected from classical arguments. The cross-correlation between the velocity and magnetic field grows as well, more so in relative terms for a stronger Hall current. We find that the helical growth rates vary exponentially with ϵ_H, provided the ion inertial scale resides within the inverse cascade range. These exponential variations are recovered phenomenologically using simple scaling arguments. They are directly linked to the wavenumber power-law dependence of generalized and magnetic helicity, $\sim k^{-2}$, in their inverse ranges. This illustrates and confirms the important role of the interplay between large and small scales in the dynamics of turbulent flows.

Keywords: Turbulence; Helicity; Inverse cascades; Hall Magnetohydrodynamic (Hall-MHD)

1. Introduction

1.1. The Interactions of Turbulent Eddies and Waves in Atmospheric and Oceanic Flows

Turbulence and nonlinear phenomena are characterized by stochastic behavior, nonlinear waves, power-law energy spectra, and by intermittent events with non-Gaussian probability distribution functions [1–6]. They are present in a multitude of geophysical and astrophysical environments (see, e.g., the recent reviews in the Special Issue of Earth & Space Science (2019) entitled "Nonlinear Systems in Geophysics: Past Accomplishments and Future Challenges"). More specifically, the role of turbulence has been advocated, for example, in the process of rain formation [7], because of strong local accelerations, in the properties of atmospheric aerosols [8], or more recently in the multi-fractality of temperature distributions [9–11]. Similarly, huge variations of the energy dissipation take place locally in the ocean [12] in the vicinity of ridges, as well as in space plasmas such as the solar wind and beyond [13] (see below, Section 1.2). Extreme events are, in general, at small scales, appearing in the gradients of the velocity, the density, the temperature and the magnetic field, through vorticity, shear

layers, filaments, or current sheets. They can also be observed at large scales, as for example with the vertical velocity in the nocturnal, very stable, Planetary Boundary Layer [4,14].

Similarly, the influence of gravity waves over turbulent eddies has been studied over Antarctica (see, e.g., [15]), and intense gradients are identified as well in that region of the globe [16]. In fact, strong vertical winds, as well as vertically sheared horizontal winds, can be viewed as common features of stably stratified turbulence [17], in the presence or not of rotation. Even though such a behavior takes place in a narrow range of the control parameter [18], it affects measurably the overall dynamics of the flow, with a slow return to isotropy at small scale [2,19,20], together with strong localized mixing, dissipation, and intermittency for Richardson numbers close to the threshold of linear or convective instabilities [20–22]. Furthermore, the trajectories of Lagrangian particles are also measurably modified in the vicinity of shear layers (see, e.g., [23]). Such a marginal state close to a threshold almost everywhere can be modeled through simplified dynamical systems following field gradients [17,18,22,24], in line with classical approaches in turbulence, as reviewed, e.g., in [25].

Finally, in the presence of rotation in a stably stratified fluid, several other phenomena can take place. The dynamical exchanges between waves and nonlinear eddies lead to a modified distribution of energy between the kinetic and potential modes, with the dominance of one over the other shifting at a wavenumber that does not depend on the Reynolds number but rather on the Froude number, that is, the ratio of the wave period to the eddy turn-over time [26] (see [27] for the case of the inverse cascade of energy). Furthermore, the existence of bidirectional dual cascades of energy towards large scales and small scales, both with constant energy fluxes, is a clear mechanism coupling nonlinearly all scales and affecting the resulting dissipation. Thus, the dynamical interactions between small and large scales play an essential role in estimating the efficiency of mixing in such flows [28–30], and it is found to vary linearly with the control parameter, namely, the Froude number [31,32].

1.2. The Case of Space Plasmas

Similar phenomena are observed as well for turbulent flows in the presence of magnetic fields. Such fields, together with charged particles, are abundant in the cosmos. At large scales, the magnetohydrodynamic (MHD) approximation, in which the displacement current is neglected in Maxwell's equations, is adequate, and observations of the solar wind, dating back to the Voyager spacecraft, confirmed the physical description of a medium governed by the interactions of turbulent, nonlinear eddies and Alfvén waves (see, e.g., for recent reviews, [33–36] and references therein). Turbulence is also found to play a central role in shaping these media [37–39].

However, as the direct turbulent cascade of energy approaches smaller scales, plasma effects and dispersive waves come into effect, appearing for example through a generalized Ohm's law whose expression depends on the degree of ionization of the medium, which itself can differ greatly from the solar wind to the interstellar gas. Current spacecraft technologies allow for the resolution of much smaller temporal and spatial scales than what was available previously, and one can now reach the ion inertial length, ϵ_H, and perhaps the electron inertial length (see for definitions the next section, and, e.g., [40]). Other types of waves, for example, kinetic Alfvén waves or whistler waves, come into play between the ion and electron scales, and the distribution of energy among modes is altered from a spectrum close to that of Kolmogorov (1941) to substantially steeper scaling laws [41], leading to marked anisotropies [42]. Using the magnetospheric multi-scale (MMS) suite of four satellites, recent observations indicate the presence of Kelvin–Helmoltz instabilities at large scales. They can drive small-scale turbulence through secondary instabilities (see, e.g., [43]), reconnection, and dissipative processes in shear layers and current sheets. The signature of Kelvin–Helmoltz instabilities and intermittency may well persist in the statistics of such flows [44]. At even smaller scales, Hall-MHD, as well as electron dynamics, are also observed [45–48]. Two-dimensional two-fluid Hall-MHD simulations have shown recently that there is a sizable proportion of the turbulent transfer, and therefore of the dissipation, that is, localized in coherent structures such as current sheets which are thin but have transverse dimensions of the order of the integral scale [49]. Besides losing energy to

dissipative processes, plasmas also exchange energy with particles through, e.g., ion-cyclotron waves, as observed recently in the magnetosphere [50].

In the presence of forcing acting only in the momentum equation, and for small initial magnetic fields, one is faced with the so-called dynamo problem of generation of magnetic fields, as reviewed extensively, e.g., in [51]. Searching for the effect of plasma waves on the growth of both large-scale and small-scale magnetic fields, one finds that, for Hall-MHD, the magnetic field grows faster for intermediate values of the control parameter ϵ_H, also with a dependence on the magnetic Reynolds number, $R_M = U_0 L_0/\eta$ with U_0, L_0 characteristic velocity and length scales, and η the magnetic diffusivity. Specifically, the growth rate is larger when the ion length scale ϵ_H is close to (but larger than) the dissipation scale (see, for example, [52,53] and references therein). Both magnetic helicity and magnetic energy grow, with a flat energy spectrum at large scales and closer to a Kolmogorov spectrum at small scales. Numerous studies have been devoted to the full dynamics of Hall MHD. For example, it is shown in [54], using shell models that the energy spectrum changes from a classical Kolmogorov law for large eddies to a steeper scaling after the ion inertial length, the slope of which depends on the amount of excess magnetic energy compared to its kinetic counterpart (see also [55] for a weak turbulence approach).

Small-scale dynamics in Hall MHD, and how its evolution differs from the pure MHD case, is of prime importance for laboratory and space plasmas, and has been studied extensively. At early times, like in MHD, vorticity and current sheets form, of thickness the dissipation length scale, called the Kolmogorov scale in fluid turbulence and with a $-3/4$ dependence on the kinetic Reynolds number $R_V = U_0 L_0/\nu$ with respect to the characteristic length scale of the flow, with ν the kinematic viscosity. These sheets can roll-up, with a strong local correlation between the velocity, the magnetic field and the current [56]. However, the dissipative scale for MHD is much smaller, for astrophysical Reynolds numbers which are very large, than the ion and even the electron inertial scales which are reached first in the process of transferring the energy to smaller scales. This leads to a second inertial range in which the nonlinearity associated with the Hall current now prevails giving different scaling laws for energy spectra. A detailed analysis of dissipative processes in space plasmas can be found in [57,58]. For example, Reynolds numbers for the solar wind, the magnetosheath, and magnetotail can vary from 10^{11} to 10^{14}. For length scales between a few to a thousand Earth's radii, this leads to a (Kolmogorov) dissipation length scale varying from the mm, i.e., comparable to the case of the atmosphere, to the meter. These scales are much smaller than the ion gyroradius, estimated to be between 70 km and 400 km, or even the electron gyroradius. This results in a substantial change in the dynamics of the flow at small scales, compared to MHD, giving rise to more complex small-scale structures, enhanced reconnection, and a steepening of energy spectra, as observed in the solar wind [41], in models [54], and in numerical simulations [59,60]. We also note that, in the presence of a strong uniform magnetic field, it is shown in [61] that the magnetic energy and helicity spectra are constrained by a relation stemming from their conservation, providing a lack of uniqueness in power-law steady-state solutions (see [62] for the case of the cross-correlation between the velocity and magnetic field in MHD). Finally, in [63], it was shown that, for the small-scale behavior of Hall MHD in the decaying case, magnetic energy becomes dominant at sub-ionic scales, with narrow and intense current structures in which one observes a strong alignment between the current and the magnetic field (leading to force-free fields), as well as a narrow electric field autocorrelation function.

On the other hand, the large-scale behavior of Hall-MHD, close to the ion inertial scale, has been much less investigated. Thus, in this paper, we wish to address the specific problem of the possible occurrence and strength of inverse cascades to large scales in Hall MHD, as we vary the ion inertial length. The next section discusses equations and parameters, and we analyze our results in Section 3 for temporal data, and in Section 4 for growth rates and spectral data. We recover some of the scaling results using simple phenomenological arguments in Section 5, and in Section 6 we briefly describe the effect of varying the ratio of the forcing scale to the ion inertial length. Finally, the last section presents a short discussion and conclusion.

2. Problem Set-Up

2.1. Equations and Parameters

For a two-species plasma made of ions and electrons, the usual Ohm's law relating electric field **E** and current density $\mathbf{j} = \nabla \times \mathbf{b}$ have to be generalized [64,65], depending on the length scale of the gradients vis-à-vis the ion inertial length scale ϵ_H, and where you could have collisionless dissipation mechanisms that limit the gradients that are formed even in the quasi-absence of collisions as in space plasmas (see [66] for the three-fluid case including neutrals). In the Hall MHD model examined here, with **v** the velocity field and η the magnetic diffusivity, the generalized Ohm's law is given by

$$\mathbf{E} = -\mathbf{v} \times \mathbf{b} + \epsilon_H \mathbf{j} \times \mathbf{b} + \eta \mathbf{j} \, . \tag{1}$$

Small-scale dynamics becomes more complex than in MHD, with the breaking of current sheets beyond the ion inertial length (see, for example, [67]). In the case of Hall MHD, a large number of studies have found that the formation of helical coherent structures is enhanced [68], as well as small-scale filamentation [69]. The Hall current can also affect the rate of growth of the magnetic field and its saturation level [70,71], as well as the level of backscatter to large scales [72]. Recent high-resolution, multi-spacecraft measurements from MMS have enabled the direct measurement of generalized Ohm's law near small-scale current sheets in greater detail than previously possible [73–75].

In this context, we write the forced incompressible Hall MHD equations, with $\nabla \cdot \mathbf{v} = 0$, $\nabla \cdot \mathbf{b} = 0$, as

$$\frac{\partial \mathbf{v}}{\partial t} = -\mathbf{v} \cdot \nabla \mathbf{v} - \nabla P + \mathbf{j} \times \mathbf{b} + \nu \nabla^2 \mathbf{v} + \mathbf{f}_v, \tag{2}$$

$$\frac{\partial \mathbf{b}}{\partial t} = \nabla \times (\mathbf{v} \times \mathbf{b}) - \epsilon_H \nabla \times (\mathbf{j} \times \mathbf{b}) + \eta \nabla^2 \mathbf{b} + \mathbf{f}_b. \tag{3}$$

The energy input in the system, modeled by $\mathbf{f}_v$ and $\mathbf{f}_b$ at small (electron) scales, can occur through reconnection processes which have been observed in the Earth's magnetotail at these scales [76]. We also note that the magnetic field **b** is in fact in units of an Alfvén velocity, with $\mathbf{b} = \mathbf{B}/\sqrt{\mu_0 \rho}$, where $\mathbf{B}, \rho_0, \mu_0$ are, respectively, the magnetic induction, the density (assumed constant), and the permeability of vacuum. The velocity **v** and magnetic field **b** are adimensionalized by a characteristic velocity U_0; P is the particle pressure, and we take $\nu = \eta$ (unit magnetic Prandtl number). Finally, $\mathbf{f}_{v,b}$ are forcing functions with random phases constrained so as to set the initial relative amount of kinetic and magnetic helicity—σ_V and σ_M—as desired (see Equation (6) below). The initial conditions are identical to the forcing formulation. We also define the magnetic potential **a**, as usual, through $\mathbf{b} = \nabla \times \mathbf{a}$. The Hall term is controlled by the dimensionless parameter $\epsilon_H = d_i$, which is the ion inertial length, measured in terms of the overall dimension of the flow (see [40] for the role of the ion scale in the overall dynamics in numerical approaches). The MHD equations are recovered for $\epsilon_H = 0$.

The code we use is pseudo-spectral and implements a hybrid methodology for parallelization, using both MPI and Open-MP [77,78], as well as GPUs [79]. The runs analyzed in this paper, computed in a cubic box with periodic boundary conditions, are summarized in Table 1. The box is of length 2π, corresponding to a minimum wavenumber $k_{min} = 1$; we use a classical 2/3 de-aliasing rule, and thus the maximum wavenumber is $k_{max} = N_p/3$ with N_p the number of grid points in each direction. The amplitude of the forcing is set so that the *rms* velocity and magnetic fields are of order unity. The time step for all the runs varies between 5×10^{-4} and 5×10^{-3}.

2.2. The Ideal Case

The ideal invariants in Hall-MHD [80], for $\nu = \eta = 0$, are the total energy $E_T = E_V + E_M = \langle |\mathbf{v}|^2 + |\mathbf{b}|^2 \rangle /2$, the magnetic helicity $H_M = \langle \mathbf{a} \cdot \mathbf{b} \rangle /2$ and the generalized helicity H_G defined as

$$H_G = \frac{1}{2} \langle (\mathbf{a} + \epsilon_H \mathbf{v}) \cdot (\mathbf{b} + \epsilon_H \boldsymbol{\omega}) \rangle = H_M + 2\epsilon_H H_C + \epsilon_H^2 H_V = H_M + \epsilon_H H_X \, . \tag{4}$$

Table 1. List of the runs with their identification ID. N_p the numerical resolution; ν the viscosity; ϵ_H the Hall parameter; $\sigma_{M,V,C,G}$ the relative rates, for the forcing, of the magnetic, kinetic, cross, and generalized helicities, respectively (see Equation (6)). Finally, Re is the Reynolds number, and $k_{d_i} = 1/\epsilon_H$ is the ion inertial wavenumber. For these runs, the forcing scale k_F is in the range $19 \leq k_F \leq 21$.

ID	N_p	ν	ϵ_H	σ_M	σ_V	σ_C	σ_G	Re	k_{d_i}
AM1	128^3	0.016	0.0	0.65	0.131	−0.027	–	15.1	–
AH2	128^3	0.016	0.0667	0.65	0.131	−0.027	0.295	17.2	15
AH3	128^3	0.016	0.0833	0.65	0.131	−0.027	0.247	17.6	12
AH4	128^3	0.016	0.14	0.65	0.131	−0.027	0.174	18.5	7
AH5	128^3	0.016	0.2	0.65	0.131	−0.027	0.15	18.8	5

In Equation (4), $\boldsymbol{\omega} = \nabla \times \mathbf{v}$ is the vorticity, $H_V = \langle \mathbf{v} \cdot \boldsymbol{\omega} \rangle / 2$ the kinetic helicity (an invariant for ideal neutral fluids), and $H_C = \frac{1}{2} \langle \mathbf{v} \cdot \mathbf{b} \rangle$ is the cross-correlation between the velocity and magnetic fields. Note that, because H_M is itself invariant, the combination $H_X = 2H_C + \epsilon_H H_V$ is also invariant. For $\epsilon_H \to 0$ corresponding to the MHD case, one thus recovers from the invariance of H_X the cross-helicity invariance which can thus be seen as the equivalent of H_X but for MHD. This change of invariants from the MHD case may imply as well a change in the dynamics of the flow (see, e.g., [81]). Note that in the expression of $H_{G,M}$ appear polarized waves (right and left, respectively); namely, H_G can be written as $H_G = \boldsymbol{\Gamma} \cdot \boldsymbol{\Omega}/2$, with $\boldsymbol{\Gamma} = \mathbf{a} + \epsilon_H \mathbf{v}$, $\boldsymbol{\Omega} = \mathbf{b} + \epsilon_H \boldsymbol{\omega} = \nabla \times \Gamma$ [82]; H_G is also called ion helicity in [83].

When MHD flows in the solar wind are strongly correlated, accelerated particles are more prominent [84]; this is likely due to the role played by H_C in the so-called exact laws for MHD [85] (see [38] for an observation of such laws, and see below, Equation (5) for the helical case in Hall MHD). It has also been conjectured that H_C can be measured in the solar convection zone [86]. Moreover, the cross-helicity in MHD is known to grow with time [87], and it has been shown to be of different signs in the large and small scales, with the so-called pinning effect at the dissipation scale [88] (see also [89]). This dichotomy is also present in the spatial structures of the flow [90], with large one-signed lobes of high relative correlation separated in the current sheets by fast oscillating structures [91]. In fact, a recent observation using the Parker Solar Probe has found changes in the sign of the cross-helicity. These are associated with magnetic switchbacks within small-scale reconnection sites in the inner heliosphere [92], as already discussed in [88,91]. Thus, H_C can affect both the large scales, and therefore be a factor in the dynamo effect of generation of large-scale magnetic fields [93], as well as play a role in the small scales modeled through an enhanced magnetic diffusivity, which can be associated with fast reconnection [94,95]. Whether H_G plays corresponding roles for scales smaller than ϵ_H has only been studied recently [96,97]. For example, on the basis of statistical equilibria, it is shown in [96] that the direction of the cascade for H_G is ambiguous, as we also argue below noting its dependence on the ion inertial length, ϵ_H.

Furthermore, the presence of cross-helicity in MHD can lead to different energy spectra, depending on σ_C (see Equation (6) below) [88,98]. Today, this remains a disputed issue which may depend on the model that is used. A unifying framework, for a two-dimensional formulation of reduced MHD in the presence of a strong uniform magnetic field, from large (MHD) scales to scales below the ion inertial length, has been proposed in [89], with, in particular, a detailed analysis of the weak (wave) turbulence regime leading to integro-differential equations with various steady power-law solutions.

Exact scaling laws in terms of structure functions can be derived for Hall MHD. They represent, in a different form, the conservation of E_T, H_M and H_G [82]. For strong Hall currents, and assuming homogeneity (but not isotropy in this formulation), these exact laws reduce to

$$\tilde{\epsilon}_m = \epsilon_H [\delta[\mathbf{b} \times \mathbf{j}] \cdot \delta \mathbf{b}] \,, \quad \tilde{\epsilon}_G = \epsilon_H [\delta[\mathbf{v} \times \mathbf{b}] \cdot \delta \boldsymbol{\omega} + \delta[\mathbf{v} \times \boldsymbol{\omega}] \cdot \delta \mathbf{b}] + \epsilon_H^2 \delta[\mathbf{v} \times \boldsymbol{\omega}] \cdot \delta \boldsymbol{\omega} \,, \tag{5}$$

where, for any vector $\mathbf{F}$, one defines $\delta\mathbf{F} = \mathbf{F}(\mathbf{x}+\mathbf{r}) - \mathbf{F}(\mathbf{x})$, with $\mathbf{r}$ in the inertial range(s), and $\tilde{\epsilon}_{[m,G]}$ are the decay rates of $H_{[M,G]}$. Such exact laws for incompressible Hall MHD, under the further assumptions of large Reynolds number and stationarity, represent dynamical constraints on the temporal, spatial and spectral evolution of the flow, that differ from the MHD case, in particular emphasizing a stronger involvement than in MHD of the small scales, through the kinetic helicity.

Finally, we define relative helicities which correspond to the relative alignment or anti-alignment of vectors when maximal (± 1); they are in fact cosines functions, namely,

$$\sigma_M = \frac{\mathbf{a}\cdot\mathbf{b}}{|\mathbf{a}||\mathbf{b}|}, \qquad \sigma_C = \frac{\mathbf{v}\cdot\mathbf{b}}{|\mathbf{v}||\mathbf{b}|}, \qquad \sigma_G = \frac{(\mathbf{a}+\epsilon_H\mathbf{v})\cdot(\mathbf{b}+\epsilon_H\boldsymbol{\omega})}{|\mathbf{a}+\epsilon_H\mathbf{v}||\mathbf{b}+\epsilon_H\boldsymbol{\omega}|} = \frac{\boldsymbol{\Gamma}\cdot\boldsymbol{\Omega}}{|\boldsymbol{\Gamma}||\boldsymbol{\Omega}|}, \qquad \sigma_V = \frac{\mathbf{v}\cdot\boldsymbol{\omega}}{|\mathbf{v}||\boldsymbol{\omega}|}\,. \quad (6)$$

In the linearized case, two types of waves coexist in Hall MHD [99]. Magnetic polarization is defined as $P_M = \sigma_M\sigma_C$, computed in Fourier space. It measures the direction of circular polarization relative to the magnetic field. $P_M > 0$ (vs. $P_M < 0$) corresponds to left (vs. right) circularly polarized fields [100]. They are called ion-cyclotron and whistler waves, and have different dispersion relations in terms of wavenumbers, which can affect the destabilization of large-scale magnetic fields, as described by the so-called alpha-dynamo in MHD. The turbulent diffusivity is affected as well by the Hall current and can become negative, unlike the MHD case in three dimensions (see [72] and references therein). The wavenumber-dependent ratio of magnetic to kinetic energy, at each wavenumber k, depends on ϵ_H and k, and the Alfvénic state of equipartition typical of MHD is broken by the Hall current, both at large scales and at small scales.

The behavior of dissipation-less ideal systems can be obtained from first principles [101–103], with the long-time energy spectrum scaling corresponding to an equipartition between all individual Fourier modes in the simplest case. However, it has been conjectured, and it has been shown recently numerically, that the behavior in the ideal case can be in fact a predictor of their dissipative counterparts, the small-scale thermalized modes acting as an effective viscosity and resistivity on the large scales [104]. Henceforth, a Kolmogorov spectrum typical of fluid turbulence, and as found in atmospheric flows [105], including for helicity [106], is observed in ideal systems at intermediate scales and intermediate times before the system reaches equilibrium. These results have been extended to other systems, as for example in MHD [107], and they are believed to be universal [108].

It is thus of great interest to study such equilibria, which can, in particular, give indications on the directions of turbulent cascades to either small or large scales. Statistical equilibria for Hall MHD with a finite number of modes were derived in [81] (see also [109]), revealing several distinguishing features of these idealized systems. In particular, there is, as in MHD, a large-scale condensation, here of generalized helicity H_G, as well as of H_M, and, to a lesser extent, also present in the magnetic energy. Furthermore, the equipartition between kinetic and magnetic energy, associated with the presence of Alfvén waves, is broken in the presence of non-zero H_G, at a wavenumber that depends on $\epsilon_H^{-1/2}$. One can conjecture that, similarly, the helical equipartition (between kinetic and current helicity) is broken, when applying a Schwarz inequality. Following up with numerical simulations, these authors also show that large-scale excitation is weaker in Hall MHD with correspondingly more small-scale energy available for dissipative processes [81]. Note that in the statistical equilibria solutions, the expressions for H_M and H_G are polynomial in ϵ_H. One can thus expect, indeed, that there will be different regimes depending on the generalized temperatures associated with these ideal invariants.

3. Large-Scale Dynamics of Hall MHD: Temporal Data

We now examine the behavior of the runs of Table 1 with small-scale forcing. We first plot, in Figure 1, the temporal variations of the total energy (Figure 1a) and the total dissipation $\epsilon_T = \epsilon_V + \epsilon_M = \nu\left\langle|\boldsymbol{\omega}|^2\right\rangle + \eta\left\langle|j|^2\right\rangle$ (Figure 1b). The different values of ϵ_H are given by different colors (see inset), and the dotted lines represent fits to the growth rates of energy (and of E_M/E_V). Note that, for all these runs, the ion inertial length is larger than the forcing scale and thus resides in the inverse

cascade range. Below these plots are given the temporal evolution of the ratio of magnetic to kinetic energy (Figure 1d) and

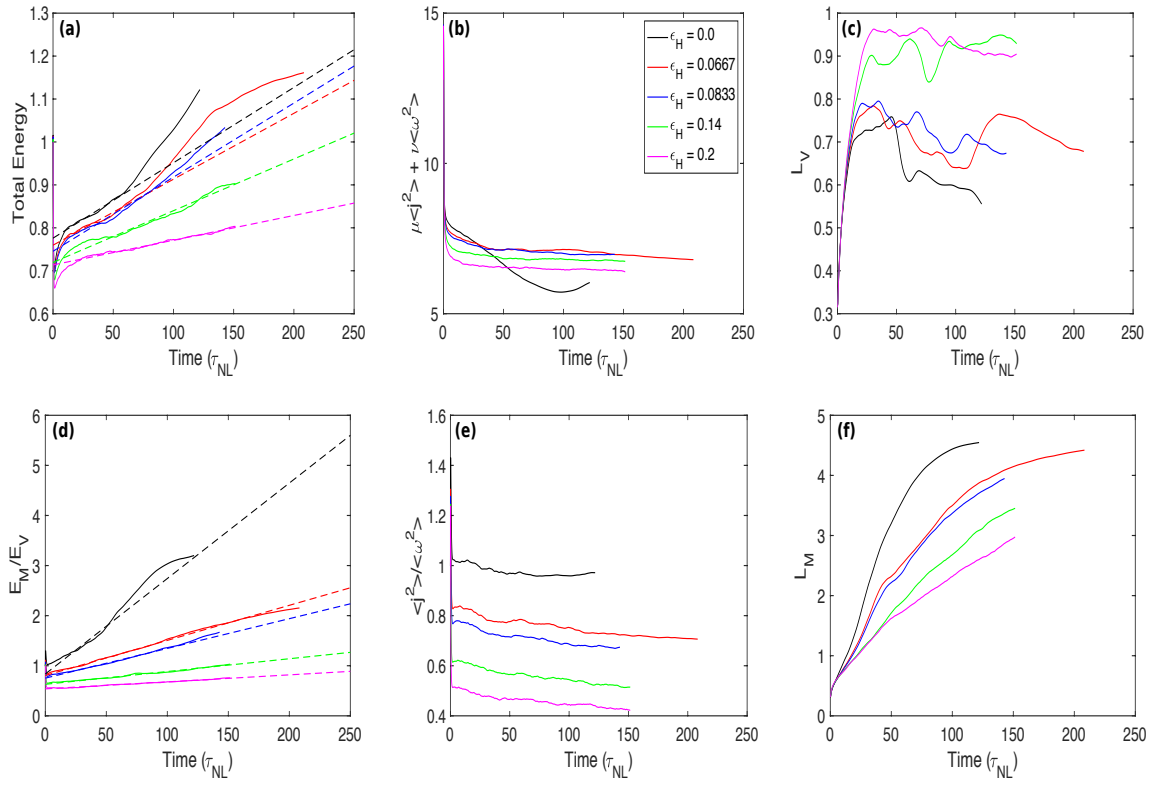

Figure 1. For runs of Table 1, as a function of time in units of turn-over time $\tau_{NL} = L_0/U_0$: Left: Total energy E_T (**a**), and ratio of magnetic to kinetic energy, E_M/E_V (**d**). Middle: Total dissipation (**b**), and ratio of L_2 norms of current and vorticity (**e**). Right: Integral scales built on the kinetic energy (**c**) and on the magnetic energy (**f**). Note the different scaling on the vertical axes. Dotted lines indicate linear fits for growth rates.

of $\langle j^2 \rangle$ / $\langle \omega^2 \rangle$ (1e). Because of the growth of H_M and H_G (see below, Figure 2), and as by Schwarz inequality, $E_M(k) \geq kH_M(k)$, E_M grows as well and thus so does E_T, as observed here. The ratio E_M/E_V also grows (Figure 1d), although to a lesser extent for the higher ϵ_H values, due to the lesser efficiency of the inverse cascade for strong Hall currents, as well as to the lack of efficient Alfvén waves. In the small scales, the saturation of dissipation in Hall-MHD is faster than in MHD, occurring at a much earlier time, and at a higher level, at least for low values of ϵ_H. Moreover, the ratio of current to vorticity, close to unity in MHD, is lower in Hall-MHD, again with a sub-dominance of dissipative eddies in current structures the stronger the Hall term (see Figure 1e).

For the highest value of ϵ_H, the energy ratio E_M/E_V remains smaller than one at all times. This corroborates the important point already noted in [81] on the basis of statistical equilibria: the Alfvén energy equipartition is broken by the Hall term. Indeed, when $\mathbf{b} = \pm\alpha\mathbf{v}$, as in an Alfvén wave, with α a pseudo-scalar constant in space, the first term in the generalized Ohm's law disappears (see Equation (1)), but the magnetic induction can still evolve through the Hall current. However, in the momentum equation, the nonlinear terms disappear altogether if as above, $\boldsymbol{\omega} = \alpha\mathbf{v}, \sigma_V = \pm 1$. This will remain true as long as current and induction do not align (we note however that, in MHD, the alignment between **b** and **j** is very efficient [110]). As ϵ_H grows, the dominance of vorticity over current can be attributed as well to the fact that the kinetic helicity term in H_G gains in importance, controlling the correlations between velocity and vorticity and thus, to some extent, the strength of the vorticity itself. Indeed, it is known that, for neutral fluids, the kinetic helicity follows a $k^{-5/3}$ law and the relative kinetic helicity thus decays slowly, as $1/k$ (for rotating flows, see [111]). The right-most

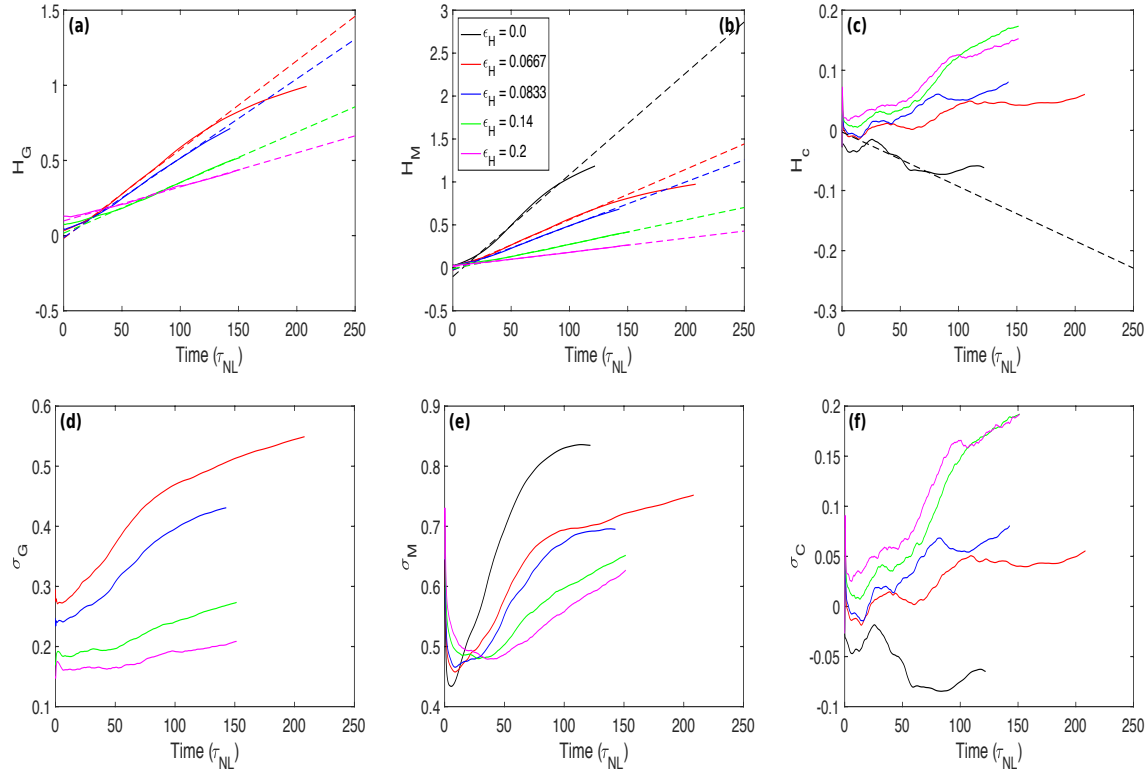

Figure 2. Temporal data for the runs of Table 1. Left column: Generalized helicity H_G (**a**) and its relative counterpart σ_G (**d**). Middle: Total magnetic helicity H_M (**b**), and its relative counterpart σ_M (**e**). Right: cross-helicity H_C (**c**), and its relative counterpart σ_C (**f**).

plots in Figure 1 give the variations with time of the magnetic (FIgure 1c) and kinetic (Figure 1f) integral scales, defined classically as:

$$L_{V,M}(t) = \frac{\int [E_{V,M}(k,t)/k]dk}{\int E_{V,M}(k,t)dk} \,. \tag{7}$$

Note the different magnitudes for L_V and L_M on the vertical axes. As for all other temporal figures, the time is in units of the turn-over time, $\tau_{NL} = L_0/U_0$. At any given time, the stronger ϵ_H, the larger L_V is, and the smaller L_M is, although for all times and all ϵ_H, L_M remains larger than L_V. This is again indicative of a lesser efficiency of the inverse cascade of magnetic helicity as the Hall term becomes more preponderant. L_V has a rapid growth, with a rate which is independent of ϵ_H, and it saturates at relatively early times, but at levels (and times) which depend on ϵ_H. On the other hand, L_M grows at rates that differ with ϵ_H and continues its growth, except for the pure MHD case. It will likely only saturate when $\sigma_M \approx 1$ at $k = k_{min} = 1$. Saturation is delayed as ϵ_H is increased, a signature of the slower growth rate for high ϵ_H.

In Figure 2, we follow-up with various helical data as a function of time for the runs of Table 1. Specifically, we display in the top row the generalized helicity (Figure 2a); the magnetic helicity, which is also an invariant in the ideal case ((Figure 2b); and the cross-helicity ((Figure 2c). Their relative rates (see Equation (6)) are given in the bottom row of Figure 2. All these helical measures grow, except for H_C in the MHD case. For H_M, the stronger growth is for MHD, and with a saturation that is reached earlier in MHD. The cross-correlation H_C grows as well, but with an inversion in the change of rate of growth with ϵ_H: there is no growth in MHD, and the growth rate of H_C increases with ϵ_H, as its role in H_G becomes more important. Another cross-correlation coefficient can be defined, namely, $\sigma'_C = H_C/E_T$ [87]. Its behavior (not shown) is almost identical to what is displayed here, for both sets of runs, and it will thus not be discussed further.

As a result, an interesting point may be the following. In MHD, it has never been quite clear whether the cross-correlation between velocity and magnetic field cascades to small scales (like the energy), or to large scales, in particular since it is not definite positive; however, its physical dimension indicates it should follow the energy itself. In the presence of inverse cascades of helicity, and using Schwarz inequalities, the magnetic energy inevitably follows the magnetic helicity [112], and so does the kinetic energy, entraining now the cross-helicity to large scales, therefore its growth. This point deserves further study. We finally note that the resulting polarization $P_m = \sigma_C \sigma_M$ is positive for all the Hall-MHD runs of Table 1, corresponding to left-polarized waves for these flows, with an increase over time from a rather low value ≈ 0.025 to close to 0.14.

The growth of the characteristic scales L_V and L_M is also noticeable when one visualizes the flow, as is done in Figure 3, which displays, at the initial and final time of the AH5 run, the relative rate of magnetic helicity (see also Figure 4 below). The imprint of the forcing scale $\approx 2\pi/20$ is seen in both plots, but at the later time, larger eddies are also clearly discernible.

4. Large-Scale Dynamics of Hall MHD: Growth Rates in Inverse Cascades and Spectral Data

Magnetic helicity is viewed as a large-scale correlation as it involves the magnetic potential; the kinetic helicity, on the other hand, favors the small scales as it involves the vorticity, whereas the cross-correlation is dimensionally comparable to the total energy. In Hall MHD, as in MHD, H_M controls the dynamics of the large scales, but H_G is hybrid scale-wise as it depends on the ion inertial length. For small ϵ_H, $H_G \approx H_M + 2\epsilon_H H_C$, and as H_M is invariant separately, so is H_C, approximately at least; thus, the inverse cascade of generalized helicity has to be less efficient since the flow dynamics also has to conserve H_C, increasingly so as ϵ_H increases. In fact, when ϵ_H becomes larger than unity, the dominant term in H_G is now the kinetic helicity which, dimensionally, is bound to have a direct cascade, as found in numerous studies of fluid turbulence. Thus, we can expect a complex dynamics of inverse cascades when ϵ_H is varied. This leads to a non-monotonic variation of the efficiency of inverse cascades in Hall MHD, as already argued by several authors, and as shown in Figure 4a in the variation of the rate of growth of generalized helicity with ϵ_H. All plots here are in lin-log coordinates. The intermediate scales embodied in H_C and the small scales embodied in H_V come into play as a constraint on the small-scale and large-scale dynamics as they become progressively relevant in this generalized helicity invariant.

As the inverse cascade proceeds, characteristic length scales increase as well, at various rates depending on the strength of the Hall term, as we saw before and as illustrated by the next plot in Figure 4b giving the variation with ϵ_H of the temporal mean of the magnetic integral scale. We also give in Figure 4 the scaling with the ion inertial length of the growth rate of the generalized helicity FIgure 4c and of its magnetic counter part Figure 4d. For this range of ϵ_H values, these growth rates both have a monotonic variation with comparable factors in the exponential decrease.

Two fits—one exponential, using $a\, e^{-b\epsilon_H}$, and one of the rational form $\alpha/(\beta+\epsilon_H)^\gamma$—are indicated in the plots with, respectively, black and red dashed lines; $1/b$ and β, like ϵ_H, have the physical dimensions of a length scale. The coefficients (a, b), (α, β, γ) are given in the insets for each fit. Note that (i) power-law indices γ are high for the two rates (between 8.8 and 10.); (ii) the fits are comparable, and in fact very close for L_M; and (iii) $b \approx \gamma$, $\alpha \approx 1$. This latter result, using a Taylor expansion, is not unexpected as long as ϵ_H remains small. However, we note that the range of values for which such fits are available is not large, preventing a better estimate of these functional forms. The expression $\alpha'/(\beta' - \epsilon_H)^{\gamma'}$ was also tried on the data. It does not fit quite as well for the helical rates of growth, but gives an equivalently good fit for L_M; however, note that this expression is singular (here, for $\epsilon_H \approx 0.79$, not shown). Finally, note that we give in the next section a phenomenological argument for the exponential form of the fits, using a simple model based on the scaling of the helicity spectra.

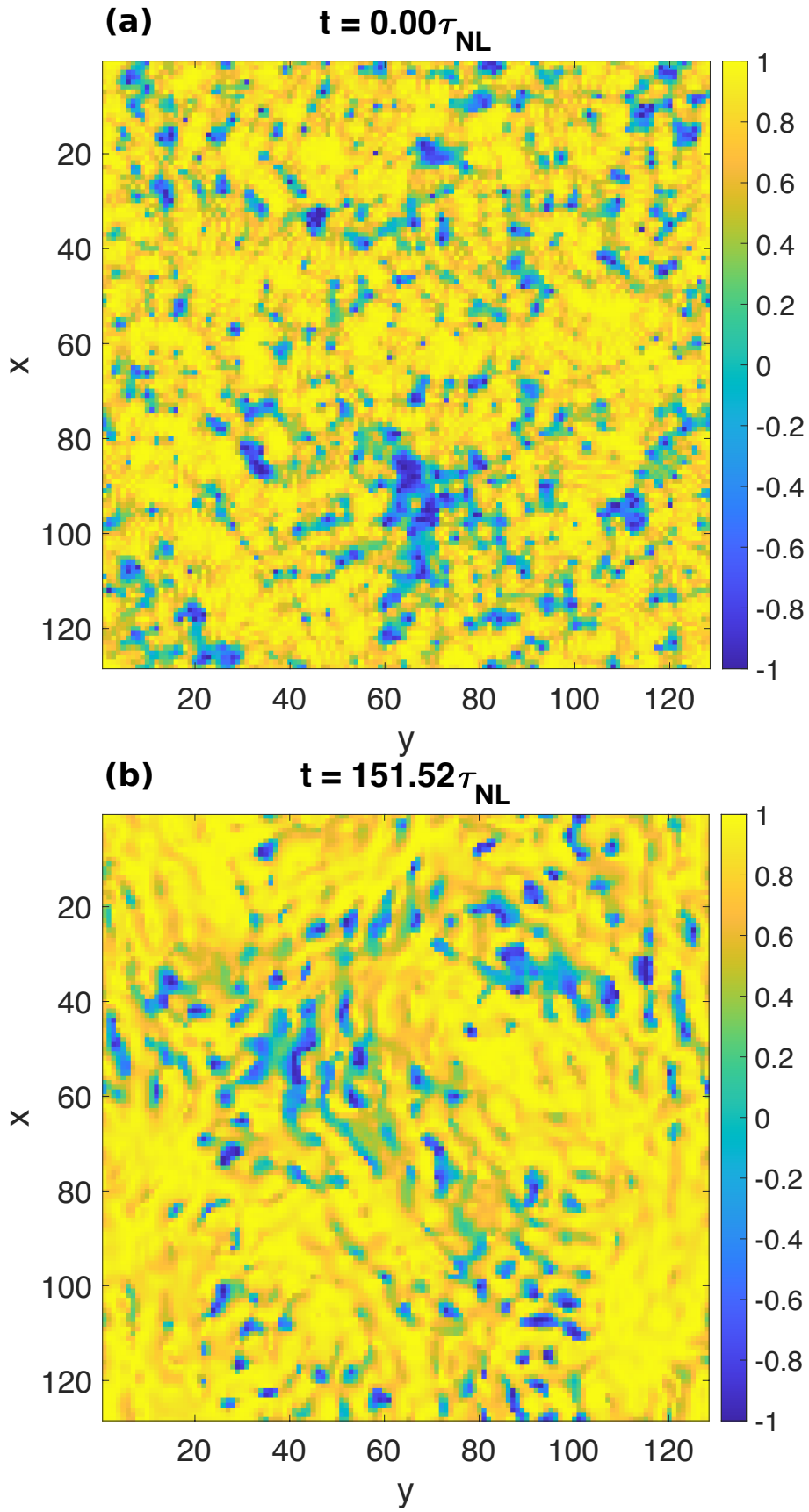

Figure 3. Horizontal cut of the pointwise relative rate of magnetic helicity $\sigma_M(\mathbf{x})$ at $t = 0$ (**a**) and at $t = 150$ (**b**) for run AH5 of Table 1, with $\epsilon_H = 0.2$ and $\sigma_M = 0.65$. The signature of the forcing, at $L_F \approx 2\pi/20 \approx 0.16$ in units of the size of the box, is visible on both plots, as well as the formation of large-scale structures at long times.

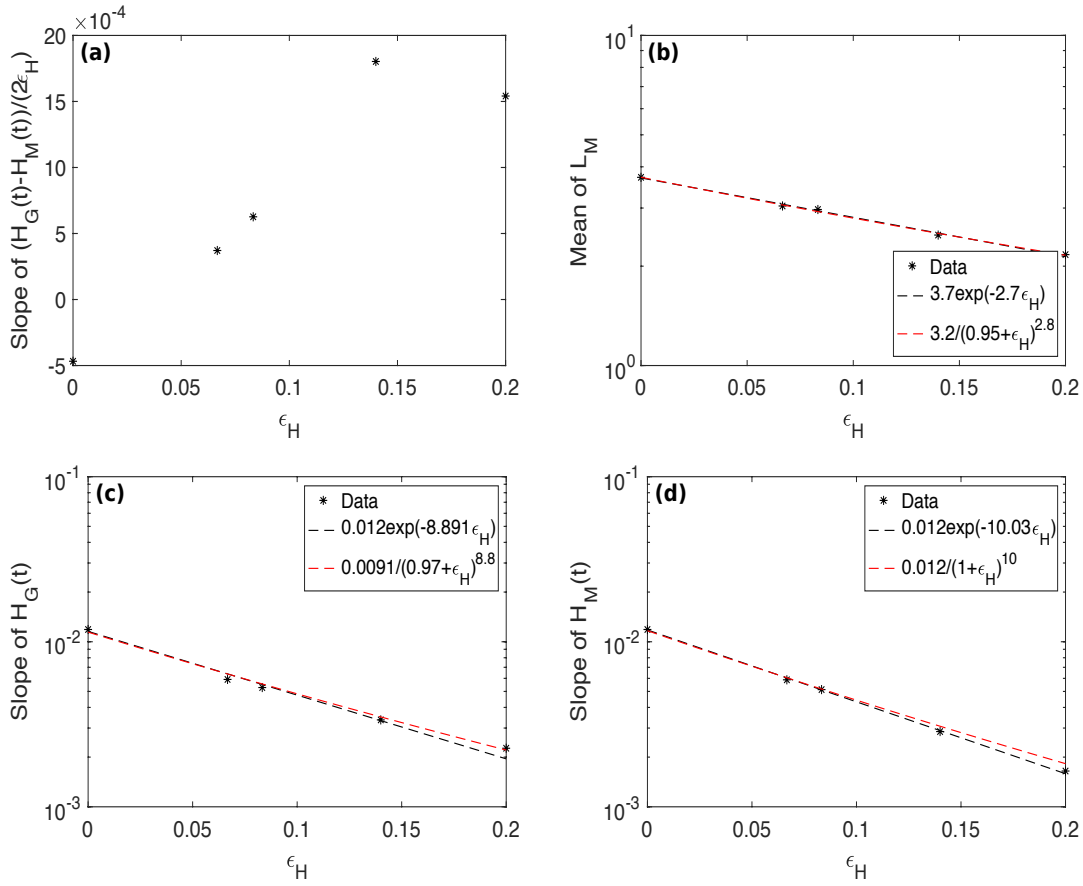

Figure 4. For the runs of Table 1, different scaling laws given as a function of ϵ_H, in lin-log coordinates. **(a)** temporal growth rate of $H_C + \epsilon_H H_V/2$ (see Equation 4). **(b)** temporal mean of the magnetic integral scale $\langle L_M \rangle_t$. **(c)** growth rate of H_G. **(d)** growth rate of H_M. When appropriate, least-square fits are done as indicated with dash lines (see insets). In black is an exponential form $a\, e^{-b\epsilon_H}$, for which a simple argument is given in Section 5, and in red, a fit to $\alpha/(\beta+\epsilon_H)^\gamma$.

Examining now spectral information, we observe that the build-up with time of the inverse cascades towards larger scales is progressive, with quasi-stationarity at intermediate scales once the inertial-range scaling is reached, as shown in Figure 5a for the generalized helicity Fourier spectrum for various times for Run AH5 of Table 1 (see insets). The k^{-2} scaling is that predicted on dimensional grounds for magnetic helicity [112] (see also next section); a Kolmogorov $-5/3$ spectrum is indicated as well, for comparison. The magnetic helicity spectra behave in similar ways (not shown). We also give in Figure 5b, and for the same times, the spectra for $H_G - H_M = \epsilon_H H_X = \epsilon_H[2H_C + \epsilon_H H_V]$, i.e., the other formulation of an helical invariant in Hall MHD. A build-up in H_X is visible as well, but with a rather flat spectrum at scales larger than but close to the forcing scale, and with a possible k^{-2} scaling at the largest scales at the latest times.

Because of a Schwarz inequality, namely, $E_M(k) \geq kH_M(k)$, the magnetic energy has to follow the magnetic helicity to large scales, as shown in Figure 5c. Moreover, we find that $E_M \sim k^{-1}$, a scaling corresponding to a fully helical state ($|\sigma_M| \approx 1$), with stationarity at intermediate scales as the inverse cascade builds up. Finally, the magnetic to kinetic energy ratio shown in Figure 5d is close to an equipartition value in the large scales, as in the case of MHD [112]; this large-scale equipartition builds up with time as the inverse cascades of both H_G and H_M proceed. On the other hand, in the small scales, magnetic energy dominates; however, no inertial range is discernible due to the lack of scale separation between $k_F \approx 20$ and the wavenumber corresponding to the grid size, $k_{max} \approx 43$. Small-scale dynamics and its possible influence on the large-scale dynamics for a sufficiently large Reynolds number will require a separate study.

5. Exponential Decrease With Hall Parameter of the Growth Rate of H_G and H_M in Inverse Cascades

As shown in the preceding sections, there is a clear growth of various physical quantities in these runs, and their growth rates vary with the magnitude of the Hall term. One striking result of Figure 4 is that we observe an exponential decay with ϵ_H of the growth rates of H_G and H_M.

These exponential scaling laws can in fact be recovered through a simple dimensional argument, which we now derive. Let us first write the equation for the temporal evolution of the magnetic helicity H_M. Pointwise, starting from Equation (3) in the absence of dissipation and forcing, we have

$$\partial_t[\mathbf{a}\cdot\mathbf{b}](\mathbf{x}) = \partial_t H_M(\mathbf{x}) = \mathbf{a}\cdot\nabla\times[(\mathbf{v}-\epsilon_H\mathbf{j})\times\mathbf{b}] + \mathbf{b}\cdot[\partial_t\mathbf{a}(\mathbf{x})]\,. \tag{8}$$

First, we remark that both terms in the time derivative of H_M contribute equally upon integration over space, and performing an integration by part; indeed, with the curl operator, there is no change of sign, namely, $\int \mathbf{m}\cdot\nabla\times\mathbf{n}\,d^3\mathbf{x} = +\int \mathbf{n}\cdot\nabla\times\mathbf{m}\,d^3\mathbf{x}$. Therefore, taking for example the Coulomb gauge, we have $D_t H_M \equiv \tilde{\epsilon}_m = 0$, and the temporal evolution of the total magnetic helicity will stem from a competition, and an eventual balance, between dissipation and forcing.

The second step is to recall the scaling of the inverse magnetic helicity cascade [112], namely,

$$H_M(k) \sim \tilde{\epsilon}_m^{2/3} k^{-2}, \tag{9}$$

with $\tilde{\epsilon}_m$ of physical dimension $[L^3][T^{-3}]$ and $\mathbf{b}$ having the dimensions of a velocity. This stems from an analysis under the assumption that the cascade is governed by $\tilde{\epsilon}_m$ and the wavenumber k, under the assumption of isotropy. This is not an entirely trivial statement, and in fact it has been proven to be irrelevant in at least two instances. On the one hand, in the neutral fluid case, the equivalent scaling based on the injection (and dissipation) rate of kinetic helicity, $\tilde{\epsilon}_v \equiv DH_v/Dt$, is $H_V(k) \sim \tilde{\epsilon}_v^{2/3}k^{-4/3}$ with $E_V(k) \sim \tilde{\epsilon}_v^{2/3}k^{-7/3}$ [113]. This scaling has never been observed, except possibly in the framework of rotating stratified turbulence as occurs in the atmosphere [114]. The generic turbulence case for fluids leads rather to a passively advected kinetic helicity with $H_V(k) \sim \tilde{\epsilon}_v\epsilon_v^{-1/3}k^{-5/3}$, where now ϵ_v is the injection rate of kinetic energy. This scaling results in a spectral relative helicity $\sigma_V(k) \sim 1/k$, corresponding to a relatively slow return to full isotropy with scale.

The second instance where the straightforward dimensional argument for the inverse cascade of helicity may be failing in some cases takes place for MHD in three dimensions: it has been shown that other spectra can be observed, differing from the k^{-2} scaling mentioned above, both at small scales and at large scales, namely, $H_M(k) \sim k^{-3}$ or steeper [115,116]. This change in the pure inverse cascade scaling may stem from non-local interactions between widely separated scales, which are strong for spectra steeper than k^{-3}. The reason for the existence of such different solutions from what is advocated in Equation (9) remains unknown at this time, although a general but somewhat a*d hoc* argument can be given to justify it on the basis of what the prevailing time-scales could be in the dynamical evolution of these systems [115,116]. This point will need further investigations.

The generalized helicity H_G has the same physical dimensions as H_M and thus the same analysis leads straightforwardly to, with $\tilde{\epsilon}_G = dH_G/Dt$:

$$H_G(k) \sim \tilde{\epsilon}_G^{2/3}k^{-2}\,. \tag{10}$$

Note that $\tilde{\epsilon}_G$ and $\tilde{\epsilon}_m$ are not independent, since $\dot{H}_G = \dot{H}_M + 2\epsilon_H\dot{H}_C + \epsilon_H^2\dot{H}_V$.

The third step in the argument to arrive at an exponential scaling is to write dimensionally, in symbolic terms, that $\tilde{\epsilon}_m \sim (a,v,b)/L_H - \epsilon_H(a,j,b)/L_H$, where L_H is a (constant) characteristic length, and where $(A,B,C) = \mathbf{A}\cdot[\mathbf{B}\times\mathbf{C}]$ (together with circular permutations) denotes a vector triple product. Note that this expression is, of course, compatible with the exact law given in Equation (5). In this simple formulation, taking the derivative with respect to ϵ_H and using the scaling of the magnetic helicity spectrum given in Equation (9), leads to the following symbolic expression written below:

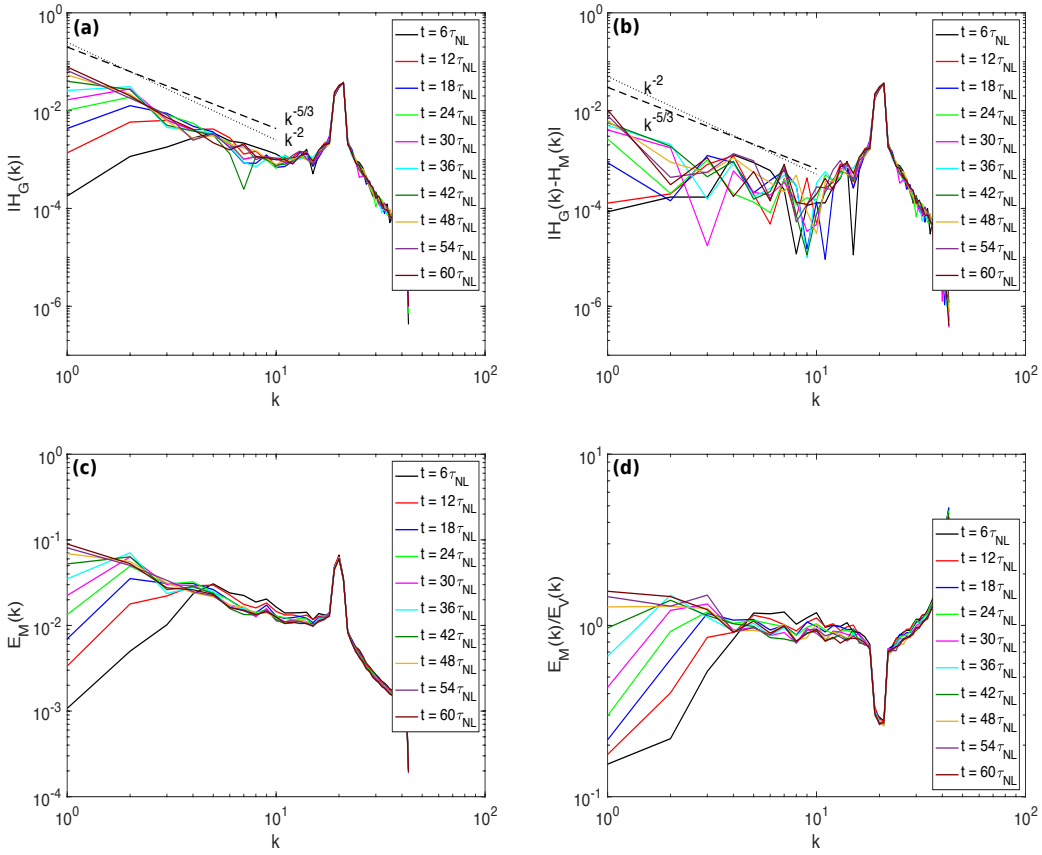

Figure 5. Top: Spectra of $H_G(k)$ (**a**) and $H_G - H_M = \epsilon_H H_X = 2\epsilon_H H_C + \epsilon_H^2 H_V$ (**b**) Bottom: Spectra of $E_M(k)$ (**c**) and $E_M(k)/E_V(k)$ (**d**) All data is for run AH5 of Table 1 at different times, in units of turn-over times. Reference power laws are also provided.

$$\frac{D\tilde{\epsilon}_m}{D\epsilon_H} \sim -\frac{(a,j,b)}{L_H} \sim -\frac{b^3}{L_H} \sim -\frac{\tilde{\epsilon}_m}{L_H}, \tag{11}$$

with the assumption that the inverse cascade of magnetic helicity is (eventually) fully helical, or $E_M(k) \sim \tilde{\epsilon}_m^{2/3} k^{-1}$, thus $E_M \sim kE_M(k) \sim b^2 \sim \tilde{\epsilon}_m^{2/3}$, neglecting logarithmic corrections. The data of Figure 2 seems indeed to indicate that $|\sigma_M|$ approaches unity for long times. From Equation (11), one then immediately obtains, with $\tilde{\epsilon}_{m,0} = \tilde{\epsilon}_m(\epsilon_H = 0)$ the rate of growth for MHD:

$$\tilde{\epsilon}_m/\tilde{\epsilon}_{m,0} = e^{-\epsilon_H/L_H}\ , \tag{12}$$

in agreement with Figure 4. Similarly, one can write

$$\tilde{\epsilon}_G/\tilde{\epsilon}_{G,0} = e^{-\epsilon_H/L_H} \tag{13}$$

for intermediate values of ϵ_H when the kinetic helicity component of H_G is still negligible. Note that these exponential behaviors all depend crucially on the scaling relationships of the magnetic and generalized helicity spectra, and on the fact that such spectra converge and thus one can express these fields locally in scale. Specifically, magnetic helicity spectra steeper than k^{-3}, as sometimes observed in MHD [115–117] and as mentioned above, would not allow for this exponential behavior.

What is L_H in the above expressions? It is likely proportional to L_F, the scale at which kinetic and magnetic energy and magnetic helicity are being injected, and the only fixed large-scale of the flow, except for $k_{min} = 1$; L_F is also the smallest scale in the inertial ranges of the inverse cascades. The empirical fit to the data (see Figure 4) indicates $L_H \approx 0.1$, whereas $L_F = 2\pi/k_F \approx 0.3$. We note that the

numerical simulations analyzed herein are performed at a constant and rather low Reynolds number, as it is well-known that the inverse cascade can develop for Reynolds number of order unity, providing the necessary nonlinearity at least at the forcing scale, and at larger scales of course. However, this supposes locality of nonlinear interactions, and this may not hold in Hall MHD as, in that case, there are interactions between small scales and large scales [72]. It also supposes that the invariant cascading to larger scales does not include smaller-scale features, which is not a correct assumption for H_G as we noted before, as it involves, for higher value of ϵ_H, the kinetic helicity. These points will thus need further studies. Another remark is that the assumption of maximal helicity may be too strong for the present case (see Figure 2).

The temporal mean of the integral scale based on the magnetic energy spectrum, L_M, on the other hand, displays a different, but still exponential, scaling. Taken over a long time after the initial growth phase, it decreases with ϵ_H (see Figure 4b). It can be seen as a consequence of the lesser efficiency of the inverse cascade of magnetic helicity as ϵ_H increases. A simple argument for this scaling goes as follows. One can show that, in the inverse cascade of magnetic helicity, the wavenumber $k(t_i)$ reached at a given time t_i is found to be proportional to [112]:

$$k(t_i) \sim [1/\tilde{\epsilon}_M^{1/3}]\, t_i^{-1}\,. \tag{14}$$

Replacing $\tilde{\epsilon}_m$ by its expression in terms of the Hall parameter ϵ_H, one can conclude that the largest scale in the system (for $k_{min} = 1$) in the Hall-MHD inverse cascade of magnetic helicity H_M, is reached at a time varying with ϵ_H as

$$T_{k_{min}=1} \sim e^{+\epsilon_H/[3L_H]}\,. \tag{15}$$

Thus, the stronger the Hall term, the longer it takes to reach the size of the box, or any scale in the inverse cascade for that matter. It follows that a temporal average of the magnetic integral scale will also decay with ϵ_H, but with a third the rate of the decrease of magnetic helicity (with possibly a logarithmic correction coming from the magnetic energy). This is consistent with what is observed in Figure 4 for both functional fits. Of course, as the excitation reaches the size of the box, the formation of large-scale coherent structures takes place. Their presence and further temporal dynamics may alter the scaling just derived, as shown recently for example in the case of two-dimensional fluids [118]. This could interfere as well with the inverse cascade scaling at late times.

Finally, we also note that we observe such an exponential variation with ϵ_H for the growth rate of $\langle a^2 \rangle$, with an exponent of ≈ -9.015 (not shown), and of the temporal rate of growth of the kinetic integral scale L_V (not shown).

6. Variation of the Forcing Wavenumber

We performed a second series of runs but now with $7 \leq k_F \leq 9$ (see Table 2). The runs are computed on grids of 48^3 points so as to preserve, comparing with the runs of Table 1, the same resolution of the small-scale dynamics. In that case, for runs with $\epsilon_H < 0.2$, the ion inertial length scale is smaller than the forcing scale and, as expected, because of the locality of nonlinear interactions in the inverse cascade, all runs see a similar growth rate, independent of ϵ_H and corresponding roughly to that of MHD (see Figure 6a). We also note that, for longer times, the saturation level of H_M does depend on ϵ_H, and is lower the larger ϵ_H, as expected from the arguments developed in the preceding section (see also [80] where it is argued that the relaxed state for long times need not be force-free in Hall MHD).

When extending these runs to higher values of ϵ_H, the ion inertial length is now again in the inverse cascade range and the growth rate of magnetic helicity is clearly smaller for higher ϵ_H (Figure 6b). This shows that the non-monotonicity in Hall-MHD, as mentioned earlier in the context of the expression of generalized helicity, is also related to the relative ratio of various significant length-scales in the problem. Finally, the variation of the growth rate of magnetic helicity with ϵ_H for all runs of Table 2 is given in Figure 7. The resulting scaling is again, in part, an exponential decrease which, when

Table 2. Same as Table 1 but with the forcing set at approximately $7 \leq k_f \approx\leq 9$. Here, for runs AH2f to AH4f, the ion inertial scale is smaller than the forcing scale, contrary to the runs of Table 1. The fit presented in Figure 6b is done for runs AH5f to AH9f.

ID	N_p	ν	ϵ_H	σ_M	σ_V	σ_C	σ_G	Re	k_{d_i}
AM1f	48^3	0.016	0.0	0.11	0.20	0.15	0.64	34.8	–
AH2f	48^3	0.016	0.0667	0.11	0.24	0.10	0.52	34.7	15
AH3f	48^3	0.016	0.0833	0.11	0.24	0.10	0.48	34.7	12
AH4f	48^3	0.016	0.14	0.11	0.24	0.10	0.36	34.7	7.2
AH5f	48^3	0.016	0.20	0.11	0.24	0.10	0.27	34.7	5
AH6f	48^3	0.016	0.25	0.11	0.20	0.15	0.23	34.8	4
AH7f	48^3	0.016	0.30	0.11	0.22	0.19	0.21	34.9	3.3
AH8f	48^3	0.016	0.45	0.11	0.20	0.15	0.15	34.8	2.2
AH9f	48^3	0.016	0.60	0.11	0.22	0.19	0.15	34.9	1.7
AH10f	48^3	0.016	0.90	0.11	0.22	0.19	0.13	34.9	1.1
AH11f	48^3	0.016	1.2	0.11	0.22	0.19	0.12	34.9	0.8

restricting ourselves to the intermediate range, has a -1.81 exponent, and with a saturation at both ends, for small or for large ϵ_H (when including all values of ϵ_H, the exponent is -1.17, not shown).

We do observe qualitatively that for a larger forcing scale, the decay has a smaller exponent, as argued in Section 5, but a quantitative agreement is clearly lacking: the scaling for the runs of Table 1 is almost five times larger than for the runs of Table 2, although the ratio in forcing scales is only a factor of 3 between the two sets of runs. Several elements could explain this discrepancy, given the fact that we argue in the preceding section that the length appearing in the scaling exponent is that of the forcing. At high values of ϵ_H, the difference is probably due to the fact that for $\epsilon_H \geq 1$, the Hall-MHD range is not fully resolved as, in that case, $L_0 = 2\pi < \epsilon_H$. Moreover, the effect of small scales in the ideal conservation laws, for H_G in particular, is felt through the contribution to its evaluation of both H_C and H_V, but nonlinear interactions at small scales are barely present in the runs of Tables 1 and 2. Indeed, another intervening factor may well be the lack of resolution of the direct inertial range in a problem in which, as ϵ_H increases, the small scales play a more prominent role in the inverse cascade through the invariance of H_G, a problem not present in pure MHD flows. Yet another factor may be the amount of cross helicity present in the flow: completely negligible for the runs of Table 1 (with $\sigma_C \approx 0.03$), it is more significant for the runs of Table 2 (with $0.1 \leq \sigma_C \leq 0.2$). As analyzed in [96], on the basis of statistical equilibria for extended MHD, the amount of cross-correlation between the velocity and the magnetic field may have a measurable effect on the strength of the inverse cascades.

7. Discussion and Conclusions

In the solar wind, the regime of Hall MHD arises at small scales, starting at the ion inertial length. It has been studied thoroughly in the context of the change to small-scale dynamics, reconnection, and dissipative processes due to the presence of dispersive plasma waves. It leads to a steepening of the energy spectra in the direct cascade, and to strong small-scale structures, all phenomena observed in the solar wind, and more recently in the magnetosheath [48,119–123]. In this paper, we are concerned with the occurrence within such a system of large-scale phenomena due to inverse cascades which are known to exist thanks to pioneering studies of idealized Hall-MHD [81]. Such inverse cascades can also affect small-scale dynamics because of the strong non-locality of global nonlinear transfer [124], even if the nonlinear interactions within the inverse cascades are local.

We show that, as a function of the ion inertial length, there is an exponential decrease of the rate of growth of magnetic and generalized helicity—H_M and H_G—as the controlling parameter for Hall MHD is increased. Moreover, this phenomenon is explained through a simple dimensional argument that relies on the scaling of the magnetic and generalized helicity spectra. Exponential scaling can also be found, in simulations of reduced MHD turbulence, for the fraction of (global) energy dissipation,

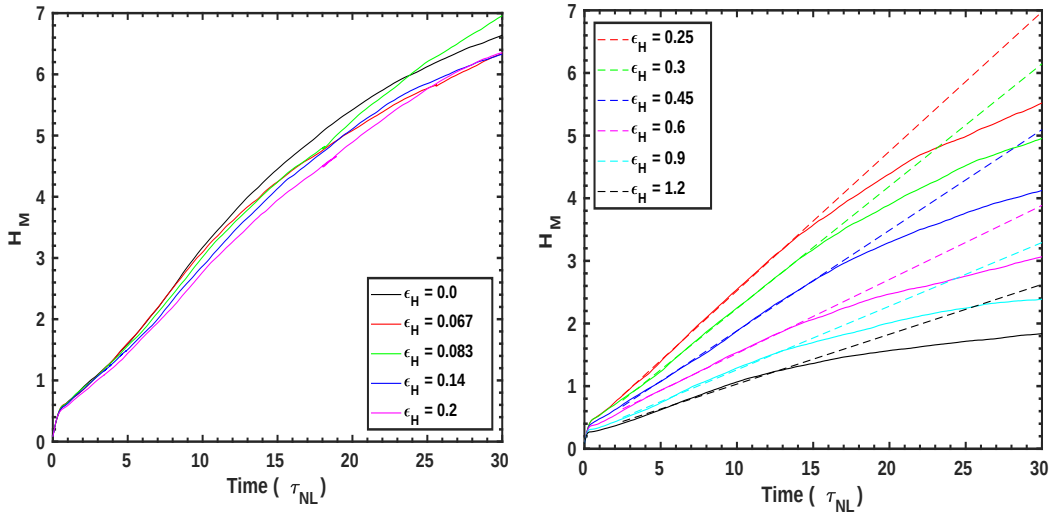

Figure 6. (a) Total magnetic helicity as a function of time measured in turn-over times for a subset of the runs of Table 2 with $k_F \approx 8$ and $\epsilon_H \leq 0.2$. **(b)** The same with values of ϵ_H extended to $\mathcal{O}(1)$ (see insets); dotted lines indicate temporal fits.

in terms of the vorticity and current (or equivalently in terms of the curl of the Elsassër variables $\boldsymbol{\omega}_\pm = \boldsymbol{\omega} \pm \mathbf{j}$), when expressed as a function of the fraction of volume occupied by dissipative structures [125].

Indeed, the subsequent energy and helicity input towards large scales can in turn affect the complex small-scale dynamics and the ensuing energy dissipation. In particular, it was stated in [81] that the inverse cascade in Hall MHD is weaker than in the MHD case, a result confirmed by the present analysis at least for positive polarity, $P_M > 0$. This can be related to the fact that, in Hall MHD, the magnetic field is not so efficient at creating a large-scale force-free structure, with a resulting $\sigma_M \approx 1$. Furthermore, it was shown in [126] for the problem of two-dimensional Navier–Stokes turbulence, that inverse transfer is effective even when no forcing is acting on the flow. This is due to the fact that, as invariants are quadratic, one has detailed balance, i.e., conservation of the invariants for each individual set of triadic interactions; as such, this represents a huge constraint on the resulting nonlinear dynamics. Therefore, the magnitude of inverse transfer in Hall-MHD, which depends on ϵ_H, is bound to affect the dissipative structures at small scales.

The correlation between the velocity and the magnetic field grows as well, in both absolute and relative terms. It is not an invariant except in the limit $\epsilon_H \to 0$, when H_X reduces to H_C (see Equation (3)). In MHD, it has been known for a long time that H_C affects the amount of dissipation present in the fluid [127], so it may be the case as well here. Furthermore, an intriguing possibility is whether or not one obtains, for some values of the controlling parameter at a given Reynolds number, a dual, bidirectional cross-helicity cascade, as already observed for the total energy in the atmosphere in the presence of both rotation and stratification [28,29]. Such two-signed constant fluxes have been found as well in oceanic data [128] and in numerical models of the atmosphere [129]. Similarly, bidirectional cascades were analyzed in the case of MHD turbulence both in two dimensions and in three dimensions (see the reviews in [30,32] and references therein). Further study of the role of H_C and of the Reynolds number in the dynamics of Hall MHD is reserved for future work. Theories of wave turbulence (or closures in the strongly nonlinear case) will be useful to achieve higher Reynolds numbers with substantial scale separation to unravel the different phenomena at play. These could also give access to formulations of

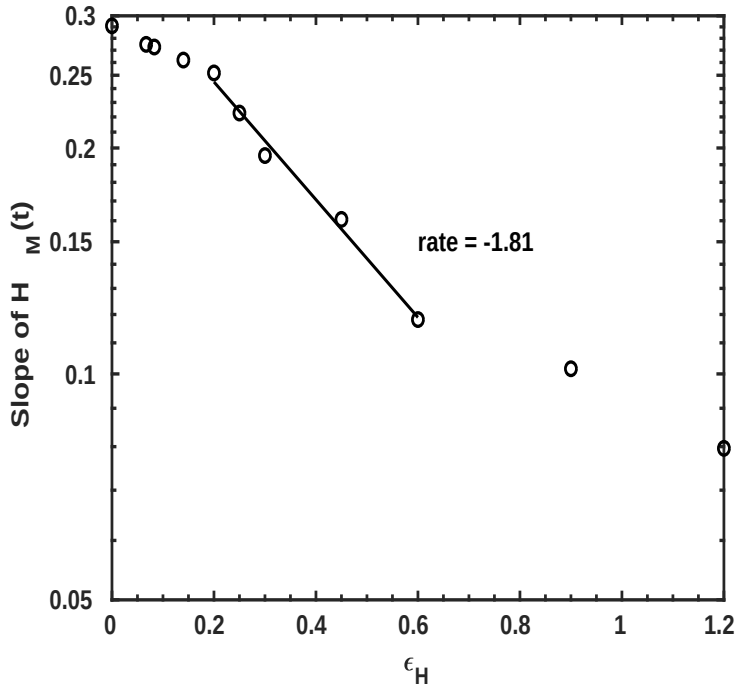

Figure 7. Variation of the rate of temporal growth of H_M with the Hall control parameter for the same runs as in Figure 6a, in lin-log coordinates. Note the three dynamical regimes, with again an exponential decay for intermediate values of ϵ_H.

transport coefficients, such as eddy viscosity and eddy noise for these complex problems, and see how they depend on the control parameters such as ϵ_H and the relative helicities. We note that, recently, a model for low ratios of magnetic to electron pressure has also detected the possibility of an inverse cascade of (generalized) cross-helicity in the context of kinetic Alfvén wave interactions [97,130] (see also [131,132]).

It would also be of interest to investigate the dynamics of inverse cascades for left-circular polarized waves, with $P_M > 0$, in which case the magnetic energy may become more prominent. It is known that the whistler waves have a stronger effect than the ion-cyclotron waves on transport coefficients and, in particular, on the effective diffusivity, which can in fact become negative [72]. Similarly, it was shown in [133] that the plasma β_P (i.e., the ratio of thermal to magnetic pressure) can affect the interactions between large and small scales and thus the inverse cascades in magneto-fluids and space plasmas. In particular, it can make them less efficient in the presence of a strong Hall current, as found here for $P_M < 0$. One could also look at these questions from the slightly less-demanding problem, from a numerical stand-point, of electron MHD (or EMHD [32,109,132,134]), in which one only deals with the evolution of the magnetic induction. EMHD is the limit of Hall MHD that obtains for small velocities and large ion inertial scales, and is known to have an inverse cascade of magnetic helicity [132,135]. For example, is the cascade in fact bidirectional? Is there more reconnection as well, due to non-local effects between large and small scales? These points are left for future work.

Author Contributions: Conceptualization, A.P. and J.S.; Data curation, J.S. and D.R.; Formal analysis, A.P.; Investigation, J.S. and D.R.; Software, D.R.; Validation, J.S. and D.R.; Visualization, J.S. and D.R.; Writing—original draft, A.P.; Writing—review & editing, A.P., J.S. and D.R. All authors have read and agreed to the published version of the manuscript.

Funding: The research contribution of JES was funded by STFC(UK) grant ST/S000364/1.

Acknowledgments: The runs analyzed in this paper have used an open allocation on the Janus super-computer at LASP/CU, which is gratefully acknowledged, together with time on a local cluster. We thank the reviewers for useful remarks. NCAR is supported by the National Science Foundation. Support for AP, from LASP and in particular from Bob Ergun, is gratefully acknowledged as well.

Conflicts of Interest: The authors declare no conflicts of interest.

References

1. Newell, A.; Nazarenko, S.; Biven, L. Wave turbulence and intermittency. *Phys. D* **2001**, *152*, 520–550.
2. Sagaut, P.; Cambon, C. *Homogeneous Turbulence Dynamics*; Cambridge University Press: Cambridge, UK, 2008.
3. Bühler, O. Wave-Vortex Interactions in Fluids and Superfluids. *Ann. Rev. Fluid Mech.* **2010**, *42*, 205–228.
4. Mahrt, L. Stably Stratified Atmospheric Boundary Layers. *Ann. Rev. Fluid Mech.* **2014**, *46*, 23–45.
5. Pouquet, A.; Marino, R.; Mininni, P.D.; Rosenberg, D. Dual constant-flux energy cascades to both large scales and small scales. *Phys. Fluids* **2017**, *29*, 111108.
6. Gregg, M.; D'Asaro, E.; Riley, J.; Kunze, E. Mixing Efficiency in the Ocean. *Ann. Rev. Marine Sci.* **2018**, *10*, 9.
7. Shaw, R.; Oncley, S.P. Acceleration intermittency and enhanced collision kernels in turbulent clouds. *Atmos. Res.* **2001**, *59–60*, 77–87.
8. Lopez, D.H.; Rabbani, M.R.; Crosbie, E.; Raman, A., Jr.; Arellano, F.A.; Sorooshian, A. Frequency and Character of Extreme Aerosol Events in the Southwestern United States: A Case Study Analysis in Arizona. *Atmosphere* **2016**, *7*, 1.
9. Lovejoy, S.; Schertzer, D. Towards a new synthesis for atmospheric dynamics: Space–time cascades. *J. Atmos.* **2010**, *96*, 1–52.
10. Kalamaras, N.; Tzanis, C.G.; Deligiorgi, D.; Philippopoulos, K.; Koutsogiannis, I. Distribution of Air Temperature Multifractal Characteristics Over Greece. *Atmosphere* **2019**, *10*, 45.
11. Schertzer, D.; Tchiguirinskaia, I. A century of turbulent cascades and the emergence of multifractal operators. *Earth Space Sci.* **2020**. DOI: https://doi.org/10.1029/2019EA000608
12. van Haren, H.; Gostiaux, L. Convective mixing by internal waves in the Puerto Rico Trench. *J. Mar. Res.* **2016**, *74*, 161–173.
13. Sorriso-Valvo, L.; Marino, R.; Carbone, V.; Noullez, A.; Lepreti, F.; Veltri, P.; Bruno, R.; Bavassano, B.; Pietropaolo, E. Observation of Inertial Energy Cascade in Interplanetary Space Plasma. *Phys. Rev. Lett.* **2007**, *99*, 115001.
14. Lenschow, D.H.; Lothon, M.; Mayor, S.D.; Sullivan, P.P.; Canut, G. A Comparison of Higher-Order Vertical Velocity Moments in the Convective Boundary Layer from Lidar with in Situ Measurements and Large-Eddy Simulation. *Bound.-Layer Meteorol.* **2012**, *143*, 107–123.
15. Cava, D.; Giostra, U.; Katul, G. Characteristics of Gravity Waves over an Antarctic Ice Sheet during an Austral Summer. *Atmosphere* **2015**, *6*, 1271–1289.
16. Walterscheid, R.L.; Gelinas, L.J.; Mechoso, C.R.; Schubert, G. Spectral distribution of gravity wave momentum fluxes over the Antarctic Peninsula from Concordiasi superpressure balloon data. *J. Geophys. Res.* **2016**, *121*, 7509–7527.
17. Rorai, C.; Mininni, P.; Pouquet, A. Turbulence comes in bursts in stably stratified flows. *Phys. Rev. E* **2014**, *89*, 043002.
18. Feraco, F.; Marino, R.; Pumir, A.; Primavera, L.; Mininni, P.; Pouquet, A.; Rosenberg, D. Vertical drafts and mixing in stratified turbulence: sharp transition with Froude number. *Eur. Phys. Lett.* **2018**, *123*, 44002.
19. Smyth, W.; Moum, J. Anisotropy of turbulence in stably stratified mixing layers. *Phys. Fluids* **2000**, *12*, 1343–1362.
20. Pouquet, A.; Rosenberg, D.; Marino, R. Linking dissipation, anisotropy and intermittency in rotating stratified turbulence. *Phys. Fluids* **2019**, *31*, 105116.
21. Smyth, W.; Nash, J.; Moum, J. Self-organized criticality in geophysical turbulence. *Sci. Rep.* **2019**, *9*, 3747.
22. Sujovolsky, N.; Mininni, P. Invariant manifolds in stratified turbulence. *Phys. Rev. Fluids* **2019**, *4*, 052402.
23. Buaria, D.; Pumir, A.; Feraco, F.; Marino, R.; Pouquet, A.; Rosenberg, D.; Primavera, L. Single-particle Lagrangian statistics from direct numerical simulations of rotating stratified turbulence. *arXiv* **2019**, arXiv:1909.12433.
24. Sujovolsky, N.; Mininni, P. From waves to convection and back again: The phase space of stably stratified turbulence. *arXiv* **2020**, arXiv:1912.03160v1.
25. Meneveau, C. Lagrangian Dynamics and Models of the Velocity Gradient Tensor in Turbulent Flows. *Ann. Rev. Fluid Mech.* **2011**, *43*, 219–245.
26. Marino, R.; Rosenberg, D.; Herbert, C.; Pouquet, A. Interplay of waves and eddies in rotating stratified turbulence and the link with kinetic-potential energy partition. *EuroPhys. Lett.* **2015**, *112*, 49001.

27. Herbert, C.; Marino, R.; Pouquet, A.; Rosenberg, D. Waves and vortices in the inverse cascade regime of rotating stratified turbulence with or without rotation. *J. Fluid Mech.* **2016**, *806*, 165–204.
28. Pouquet, A.; Marino, R. Geophysical turbulence and the duality of the energy flow across scales. *Phys. Rev. Lett.* **2013**, *111*, 234501.
29. Marino, R.; Pouquet, A.; Rosenberg, D. Resolving the paradox of oceanic large-scale balance and small-scale mixing. *Phys. Rev. Lett.* **2015**, *114*, 114504.
30. Alexakis, A.; Biferale, L. Cascades and transitions in turbulent flows. *Phys. Rep.* **2018**, *762*, 1–139.
31. Pouquet, A.; Rosenberg, D.; Marino, R.; Herbert, C. Scaling laws for mixing and dissipation in unforced rotating stratified turbulence. *J. Fluid Mech.* **2018**, *844*, 519–545.
32. Pouquet, A.; Rosenberg, D.; Stawarz, J.; Marino, R. Helicity Dynamics, Inverse, and Bidirectional Cascades in Fluid and Magnetohydrodynamic Turbulence: A Brief Review. *Earth Space Sci.* **2019**, *6*, 351–369.
33. Bruno, R.; Carbone, V. The solar wind as a turbulence laboratory. *Living Rev. Solar Phys.* **2005**, *2*, 4.
34. Veltri, P.; Carbone, V.; Lepreti, F.; Nigro, G. Self-Organization in Magnetohydrodynamic Turbulence. In *Encyclopedia of Complexity and System Science*; **2009** , R. A. Meyers Ed.; Springer: Berlin, Germany.
35. Matthaeus, W.H.; Wan, M.; Servidio, S.; Greco, A.; Osman, K.T.; Oughton, S.; Dmitruk, P. Intermittency, nonlinear dynamics and dissipation in the solar wind and astrophysical plasmas. *Phil. Trans. R. Soc. A* **2015**, *373*, 20140154.
36. Galtier, S. Turbulence in space plasmas and beyond. *J. Phys. A Math. Theor.* **2018**, *51*, 293001.
37. Matthaeus, W.; Velli, M. Who Needs Turbulence? A Review of Turbulence Effects in the Heliosphere and on the Fundamental Process of Reconnection. *Space Sci. Rev.* **2011**, *160*, 145–168.
38. Marino, R.; Sorriso-Valvo, L.; D'Amicis, R.; Carbone, V.; Bruno, R.; Veltri, P. On the occurence of the third-order scaling in high latitude Solar Wind. *Astrophys. J.* **2012**, *750*, 41.
39. Pouquet, A. On the possible role of constraints in MHD turbulence. In *Lecture Notes, Festival de Théorie, Aix-en-Provence*; Ghendrih, P., Diamond, P., Eds.; World Scientific: Singapore 2015; pp. 45–79.
40. Tóth, G.; Chen, Y.; Gombosi, T.I.; Cassak, P.; Markidis, S.; Peng, I.B. Scaling the Ion Inertial Length and Its Implications for Modeling Reconnection in Global Simulations. *J. Geophys. Res.* **2017**, *122*, 10336–10355.
41. Sahraoui, F.; Huang, S.; Belmont, G.; Goldstein, M.L.; Rétino, A.; Robert, P.; de Patoul, J. Scaling of the electron dissipation range of Solar Wind turbulence. *Astrophys. J.* **2013**, *777*, 15.
42. Lacombe, C.; Alexandrova, O.; Matteini, L. Anisotropies of the Magnetic Field Fluctuations at Kinetic Scales in the Solar Wind: Cluster Observations. *Astrophys. J.* **2017**, *848*, 45.
43. Stawarz, J.E.; Eriksson, S.; Wilder, F.D.; Ergun, R.E.; Schwartz, S.J.; Pouquet, A.; Burch, J.L.; Giles, B.L.; Khotyaintsev, Y.; Le Contel, O.; et al. Observations of turbulence in a Kelvin-Helmholtz event on 8 September 2015 by the Magnetospheric Multiscale mission. *J. Geophys. Res. Space Phys.* **2016**, *121*, 11021–11034.
44. Mare, F.D.; Sorriso-Valvo, L.; Retinò, A.; Malara, F.; Hasegawa, H. Evolution of Turbulence in the Kelvin-Helmholtz Instability in the Terrestrial Magnetopause. *Atmosphere* **2019**, *10*, 561.
45. Le Contel, O.; Retinó, A.; Breuillard, H.; Mirioni, L.; Robert, P.; Chasapis, A.; Lavraud, B.; Chust, T.; Rezeau, L.; Wilder, F.D.; et al. Whistler mode waves and Hall fields detected by MMS during a dayside magnetopause crossing. *Geophys. Res. Lett.* **2016**, *43*, 5943–5952.
46. Faganello, M.; Califano, F. Review, Magnetized Kelvin-Helmholtz instability: theory and simulations in the Earth's magnetosphere context. *J. Plasma Phys.* **2017**, *83*, doi:10.1017/S0022377817000770.
47. Bandyopadhyay, R.; Chasapis, A.; Chhiber, R.; Parashar, T.N.; Matthaeus, W.H.; Shay, M.A.; Maruca, B.A.; Burch, J.L.; Moore, T.E.; Pollock, C.J.; et al. Incompressive Energy Transfer in the Earth's Magnetosheath: Magnetospheric Multiscale Observations. *Astrophys. J.* **2018**, *866*, 106.
48. Stawarz, J.E.; Gershman, D.J.; Eastwood, J.P.; Phan, T.D.; Gingell, I.L.; Shay, M.A.; Burch, J.L.; Ergun, R.E.; Giles, B.L.; Contel, O.L.; et al. Properties of the Turbulence Associated with Electron-only Magnetic Reconnection in Earth's Magnetosheath. *Astrophys. J. Lett.* **2019**, *877*, L37.
49. Camporeale, E.; Sorriso-Valvo, L.; Califano, F.; Retinó, A. Coherent Structures and Spectral Energy Transfer in Turbulent Plasma: A Space-Filter Approach. *Phys. Rev. Lett.* **2018**, *120*, 125101.
50. Kitamura, N.; Kitahara, M.; Shoji, M.; Miyoshi, Y.; Hasegawa, H.; Nakamura, S.; Katoh, Y.; Saito, Y.; Yokota, S.; Gershman, D.J.; et al. Direct measurements of two-way wave-particle energy transfer in a collisionless space plasma. *Science* **2018**, *361*, 1000–1003.
51. Brandenburg, A.; Subramanian, K. Astrophysical magnetic fields and nonlinear dynamo theory. *Phys. Rep.* **2005**, *417*, 1–209.

52. Mahajan, S.M.; Mininni, P.D.; Gómez, D.O. Waves, Coriolis force, and the dynamo effect. *Astrophys. J.* **2005**, *619*, 1014–1018.
53. Mininni, P.D.; Gómez, D.; Mahajan, S. Direct simulations of helical Hall-MHD turbulence and dynamo action. *Astrophys. J.* **2005**, *619*, 1019–1027.
54. Galtier, S.; Buchlin, E. Multiscale Hall MHD turbulence in the Solar Wind. *Astrophys. J.* **2007**, *656*, 560–566.
55. Galtier, S. Wave turbulence in incompressible magnetohydrodynamics. *J. Plasma Phys.* **2006**, *72*, 721–769.
56. Mininni, P.; Pouquet, A.; Montgomery, D. Small-Scale Structures in Three-Dimensional Magnetohydrodynamic Turbulence. *Phys. Rev. Lett.* **2006**, *97*, 244503.
57. Borovsky, J.E.; Funsten, H.O. Role of solar wind turbulence in the coupling of the solar wind to the Earth's magnetosphere. *J. Geophys. Res.* **2003**, *108*, 1246.
58. Borovsky, J.E.; Funsten, H.O. MHD turbulence in the Earth's plasma sheet: Dynamics, dissipation, and driving. *J. Geophys. Res.* **2003**, *108*, 1284.
59. Franci, L.; Landi, S.; Matteini, L.; Verdini, A.; Hellinger, P. High-resolution hybrid simulations of kinetic plasma turbulence at proton scales. *Astrophys. J.* **2015**, *812*, 21.
60. Gonzàlez, C.A.; Parashar, T.N.; Gomez, D.; Matthaeus, W.H.; Dmitruk, P. Turbulent electromagnetic fields at sub-proton scales: Two-fluid and full-kinetic plasma simulations. *Phys. Plasmas* **2019**, *26*, 012306.
61. Galtier, S.; Meyrand, A. Entanglement of helicity and energy in kinetic Alfvén wave/whistler turbulence. *J. Plasma Phys.* **2015**, *81*, 325810106.
62. Grappin, R.; Pouquet, A.; Léorat, J. Dependence of MHD turbulence spectra on the velocity-magnetic field correlation. *Astron. Astrophys.* **1983**, *126*, 51–58.
63. Stawarz, J.E.; Pouquet, A. Small-scale behavior of Hall magnetohydrodynamic turbulence. *Phys. Rev. E* **2015**, *92*, 063102.
64. Vasyliunas, V.M. Theoretical models of magnetic field line merging. 1. *Rev. Geophys. Space Phys.* **1975**, *13*, 303–336.
65. Priest, E.; Forbes, T. *Magnetic Reconnection: MHD Theory and Applications*; Cambridge University Press: Cambridge, UK, 2000.
66. Song, P.; Gombosi, T.; Ridley, A. Three-fluid Ohm's law. *J. Geophys. Res.* **2001**, *106*, 8149–8156.
67. Cothran, C.D.; Landreman, M.; Brown, M.R.; Matthaeus, W. Generalized Ohm's law in a 3-D reconnection experiment. *Geophys. Res. Lett.* **2005**, *32*, L03105.
68. Mahajan, S.; Yoshida, Z. Double Curl Beltrami Flow: Diamagnetic Structures. *Phys. Rev. Lett.* **1998**, *99*, 4863–4866.
69. Laveder, D.; Passot, T.; Sulem, P. Transverse dynamics of dispersive Alfvén waves. I. Direct numerical evidence of filamentation. *Phys. Plasmas* **2002**, *9*, 293–305.
70. Mininni, P.; Gómez, D.O.; Mahajan, S.M. Role of the Hall current in magnetohydrodynamic dynamos. *Astrophys. J.* **2003**, *584*, 1120–1126.
71. Gòmez, D.; Mininni, P.; Dmiturk, P. Hall-magnetohydrodynamic small-scale dynamos. *Phys. Rev. E* **2010**, *82*, 036406.
72. Mininni, P.D.; Alexakis, A.; Pouquet, A. Energy transfer in Hall-MHD turbulence, cascades, backscatter and dynamo action. *J. Plasma Phys.* **2007**, *73*, 377–401.
73. Torbert, R.B.; Burch, J.L.; Giles, B.L.; Gershman, D.; Pollock, C.J.; Dorelli, J.; Avanov, L.; Argall, M.R.; Shuster, J.; Strangeway, R.J.; et al. Estimates of terms in Ohm's law during an encounter with an electron diffusion region. *Geophys. Res. Lett.* **2016**, *43*, 5918–5925.
74. Webster, J.; Burch, J.L.; Reiff, P.H.; Daou, A.G.; Genestreti, K.J.; Graham, D.B.; Torbert, R.B.; Ergun, R.E.; Sazykin, S.Y.; Marshall, A.; et al. Magnetospheric Multiscale Dayside Reconnection Electron Diffusion Region Events. *J. Geophys. Res.* **2018**, *123*, 4858–4878.
75. Shuster, J.R.; Gershman, D.J.; Chen, L.J.; Wang, S.; Bessho, N.; Dorelli, J.C.; da Silva, D.E.; Giles, B.L.; Paterson, W.R.; Denton, R.E.; et al. MMS Measurements of the Vlasov Equation: Probing the Electron Pressure Divergence Within Thin Current Sheets. *Geophys. Res. Lett.* **2019**, *46*, 7862–7872.
76. Ergun, R.E.; Goodrich, K.A.; Wilder, F.D.; Ahmadi, N.; Holmes, J.C.; Eriksson, S.; Stawarz, J.E.; Nakamura, R.; Genestreti, K.J.; Hesse, M.; et al. Magnetic Reconnection, Turbulence, and Particle Acceleration: Observations in the Earth's Magnetotail. *Geophys. Res. Lett.* **2018**, *45*, 3338–3347.
77. Mininni, P.; Dmitruk, P.; Matthaeus, W.H.; Pouquet, A. Large-scale behavior and statistical equilibria in rotating flows. *Phys. Rev. E* **2011**, *83*, 016309.
78. Mininni, P.; Rosenberg, D.; Reddy, R.; Pouquet, A. A hybrid MPI-OpenMP scheme for scalable parallel pseudospectral computations for fluid turbulence. *Parallel Comput.* **2011**, *37*, 316–326.

79. Rosenberg, D.; Mininni, P.D.; Reddy, R.; Pouquet, A. GPU Parallelization of a Hybrid Pseudospectral Geophysical Turbulence Framework Using CUDA. *Atmosphere* **2020**, *11*, 00178.
80. Turner, L. Hall effects on magnetic relaxation. *IEEE Trans. Plasma Sci.* **1986**, *PS-14*, 849–857.
81. Servidio, S.; Matthaeus, W.H.; Carbone, V. Statistical properties of ideal three-dimensional Hall magnetohydrodynamics: The spectral structure of the equilibrium ensemble. *Phys. Plasmas* **2008**, *15*, 042314.
82. Banerjee, S.; Galtier, S. Chiral exact relations for helicities in Hall magnetohydrodynamic turbulence. *Phys. Rev. E* **2016**, *93*, 033120.
83. Ohsaki, S.; Yoshida, Z. Variational principle with singular perturbation of Hall magnetohydrodynamics. *Phys. Plasmas* **2005**, *12*, 064505.
84. Sorriso-Valvo, L.; Catapano, F.; Retinò, A.; Le Contel, O.; Perrone, D.; Roberts, O.W.; Coburn, J.T.; Panebianco, V.; Valentini, F.; Perri, S.; et al. Turbulence-Driven Ion Beams in the Magnetospheric Kelvin-Helmholtz Instability. *Phys. Rev. Lett.* **2019**, *122*, 035102.
85. Politano, H.; Pouquet, A. Dynamical length scales for turbulent magnetized flows. *Geophys. Res. Lett.* **1998**, *25*, 273–276.
86. Rüdiger, G.; Kitchatinov, L.; Brandenburg, A. Cross Helicity and Turbulent Magnetic Diffusivity in the Solar Convection Zone. *Sol. Phys.* **2011**, *269*, 3–12.
87. Pouquet, A.; Meneguzzi, M.; Frisch, U. Growth of correlations in magnetohydrodynamic turbulence. *Phys. Rev. A* **1986**, *33*, 4266–4276.
88. Grappin, R.; Frisch, U.; Léorat, J.; Pouquet, A. Alfvénic fluctuations as asymptotic states of MHD turbulence. *Astron. Astrophys.* **1982**, *102*, 6–14.
89. Passot, T.; Sulem, P.L. Imbalanced kinetic Alfvén wave turbulence: from weak turbulence theory to nonlinear diffusion models for the strong regime. *J. Plasma Phys.* **2019**, *85*, 905850301.
90. Perez, J.C.; Boldyrev, S. Role of cross-helicity in magnetohydrodynamic turbulence. *Phys. Rev. Lett.* **2009**, *102*, 025003.
91. Meneguzzi, M.; Politano, H.; Pouquet, A.; Zolver, M. A sparse-mode spectral method for the simulations of turbulent flows. *J. Comp. Phys.* **1996**, *123*, 32–44.
92. McManus, M.D.; Bowen, T.A.; Mallet, A.; Chen, C.H.; Chandran, B.D.; Bale, S.D.; Livi, R.; Larson, D.E.; de Wit, T.D.; Kasper, J.; et al. Cross Helicity Reversals in Magnetic Switchbacks. *Astrophys. J. Suppl. Series* **2020**, *246*, 67.
93. Yokoi, N. Cross helicity and related dynamo. *Geophys. Astrophys. Fluid Dyn.* **2013**, *107*, 114–184.
94. Yokoi, N.; Higashimori, K.; Hoshino, M. Transport enhancement and suppression in turbulent magnetic reconnection: A self-consistent turbulence model. *Phys. Plasmas* **2013**, *20*, 122310.
95. Titov, V.; Stepanov, R.; Yokoi, N.; Verma, M.; Samtaney, R. Cross helicity sign reversals in the dissipative scales of magnetohydrodynamic turbulence. *Magnetohydrodynamics* **2019**, *55*, 225–232.
96. Milosevich, G.; Lingam, M.; Morrison, P.J. On the structure and statistical theory of turbulence of extended magnetohydrodynamics. *Astrophys. J. Lett.* **2017**, *19*, 015007.
97. Milosevich, G.; Passot, T.; Sulem, P. Modeling Imbalanced Collisionless Alfvén Wave Turbulence with Nonlinear Diffusion Equations. *Astrophys. J. Lett.* **2020**, *888*, L7.
98. Politano, H.; Pouquet, A.; Sulem, P. Inertial ranges and resistive instabilities in two–dimensional MHD turbulence. *Phys. Fluids B* **1989**, *1*, 2330–2339.
99. Sahraoui, F.; Galtier, S.; Belmont, G. On waves in incompressible Hall magnetohydrodynamics. *J. Plasma Phys.* **2006**, *73*, 723–730.
100. Meyrand, R.; Galtier, S. Spontaneous Chiral Symmetry Breaking of Hall Magnetohydrodynamic Turbulence. *Phys. Rev. Lett.* **2012**, *109*, 194501.
101. Lee, T.D. On some statistical properties of hydrodynamical and magneto-hydrodynamical fields. *Quart. Appl. Math.* **1952**, *10*, 69–74.
102. Kraichnan, R. Inertial ranges in two-dimensional turbulence. *Phys. Fluids* **1967**, *10*, 1417–1423.
103. Kraichnan, R. Helical turbulence and absolute equilibrium. *J. Fluid Mech.* **1973**, *59*, 745–752.
104. Cichowlas, C.; Bonaïti, P.; Debbasch, F.; Brachet, M. Effective Dissipation and Turbulence in Spectrally Truncated Euler Flows. *Phys. Rev. Lett.* **2005**, *95*, 264502.
105. Nastrom, G.D.; Gage, K. A climatology of atmospheric wavenumber spectra of wind and temperature observed by commercial aircraft. *J. Atmos. Sci.* **1985**, *42*, 950–960.

106. Koprov, B.; Koprov, V.; Ponomarev, V.; Chkhetiani, O. Experimental Studies of Turbulent Helicity and Its Spectrum in the Atmospheric Boundary Layer. *Dokl. Phys.* **2005**, *50*, 419–422.
107. Krstulovic, G.; Brachet, M.; Pouquet, A. Alfvén waves and ideal two-dimensional Galerkin truncated magnetohydrodynamics. *Phys. Rev. E* **2011**, *84*, 016410.
108. Mininni, P.D.; Pouquet, A. Energy spectra stemming from interactions of Alfvén waves and turbulent eddies. *Phys. Rev. Lett.* **2007**, *99*, 254502.
109. Zhu, J.Z.; Yang, W.; Zhu, G.Y. Purely helical absolute equilibria and chirality of (magneto)fluid turbulence. *J. Fluid Mech.* **2014**, *739*, 479–501.
110. Servidio, S.; Matthaeus, W.; Dmitruk, P. Depression of nonlinearity in isotropic MHD turbulence. *Phys. Rev. Lett.* **2008**, *100*, 095005.
111. Mininni, P.; Pouquet, A. Helicity cascades in rotating turbulence. *Phys. Rev. E* **2009**, *79*, 026304.
112. Pouquet, A.; Frisch, U.; Léorat, J. Strong MHD helical turbulence and the nonlinear dynamo effect. *J. Fluid Mech.* **1976**, *77*, 321–354.
113. Brissaud, A.; Frisch, U.; Léorat, J.; Lesieur, M.; Mazure, A. Helicity cascades in fully developed isotropic turbulence. *Phys. Fluids* **1973**, *16*, 1366–1367.
114. Baerenzung, J.; Mininni, P.; Pouquet, A.; Rosenberg, D. Spectral modeling of turbulent flows and the role of helicity in the presence of rotation. *J. Atmos. Sci.* **2011**, *68*, 2757–2770.
115. Mininni, P.; Pouquet, A. Finite dissipation and intermittency in MHD. *Phys. Rev. E* **2009**, *80*, 025401.
116. Müller, W.; Malapaka, S.; Busse, A. Inverse cascade of magnetic helicity in magnetohydrodynamic turbulence. *Phys. Rev. E* **2012**, *85*, 015302.
117. Müller, W.; Malapaka, S. Role of helicities for the dynamics of turbulent magnetic fields. *Geophys. Astrophys. Fluid Dyn.* **2013**, *107*, 93–100.
118. Frishman, A.; Herbert, C. Turbulence Statistics in a Two-Dimensional Vortex Condensate. *Phys. Rev. Lett.* **2018**, *120*, 204505.
119. Alexandrova, O.; Lacombe, C.; Mangeney, A. Spectra and anisotropy of magnetic fluctuations in theEarth's magnetosheath: Cluster observations. *Ann. Geophys.* **2008**, *26*, 3585–3596.
120. Huang, S.Y.; Hadid, L.Z.; Sahraoui, F.; Yuan, Z.G.; Deng, X.H. On the Existence of the Kolmogorov Inertial Range in the Terrestrial Magnetosheath Turbulence. *Astrophys. J. Lett.* **2017**, *863*, L10.
121. Chasapis, A.; Matthaeus, W.H.; Parashar, T.N.; Wan, M.; Haggerty, C.C.; Pollock, C.J.; Giles, B.L.; Paterson, W.R.; Dorelli, J.; Gershman, D.J.; et al. In Situ Observation of Intermittent Dissipation at Kinetic Scales in the Earth's Magnetosheath. *Astrophys. J. Lett.* **2018**, *856*, L19.
122. Phan, T.D.; Eastwood, J.P.; Shay, M.A.; Drake, J.F.; Sonnerup, B.U.Ö.; Fujimoto, M.; Cassak, P.A.; Øieroset, M.; Burch, J.L.; Torbert, R.B.; et al. Electron magnetic reconnection without ion coupling in Earth's turbulent magnetosheath. *Nature* **2018**, *557*, 202–206.
123. Bandyopadhyay, R.; Sorriso-Valvo, L.; Chasapis, A.; Hellinger, P.; Matthaeus, W.H.; Verdini, A.; Landi, S.; Franci, L.; Matteini, L.; Giles, B.L.; et al. In-situ observation of Hall Magnetohydrodynamic Cascade in Space Plasma. *arXiv* **2019**, arXiv:1907.06802.
124. Alexakis, A.; Mininni, P.; Pouquet, A. On the inverse cascade of magnetic helicity. *Astrophys. J.* **2006**, *640*, 335–343.
125. Zhdankin, V.; Boldyrev, S.; Uzdensky, D.A. Scalings of intermittent structures in magnetohydrodynamic turbulence. *Phys. Plasmas* **2016**, *23*, 055705.
126. Mininni, P.; Pouquet, A. Inverse cascade behavior in freely decaying two-dimensional fluid turbulence. *Phys. Rev. E* **2013**, *87*, 033002.
127. Pouquet, A.; Sulem, P.L.; Meneguzzi, M. Influence of velocity-magnetic field correlations on decaying magnetohydrodynamic turbulence with neutral X-points. *Phys. Fluids* **1988**, *31*, 2635–2643.
128. Scott, R.; Wang, F. Direct Evidence of an Oceanic Inverse Kinetic Energy Cascade from Satellite Altimetry. *J. Phys. Oceanogr.* **2005**, *35*, 1650–1666.
129. Skamarock, W.C.; Park, S.H.; Klemp, J.B.; Snyder, C. Atmospheric Kinetic Energy Spectra from Global High-Resolution Nonhydrostatic Simulations. *J. Atmos. Sci.* **2014**, *71*, 4369–4381.
130. Passot, T.; Sulem, P.L.; Tassi, E. Gyrofluid modeling and phenomenology of low-β_e Alfvén wave turbulence. *Phys. Plasmas* **2018**, *25*, 041207.
131. Schekochihin, A.; Cowley, S.; Dorland, W.; Hammett, G.; Howes, G.; Quataert, E.; Tatsuno, T. Astrophysical gyrokinetics: Kinetic and fluid turbulent cascades in magnetized weakly collisional plasmas. *Astrophys. J. Suppl.* **2009**, *182*, 310.

132. Cho, J. Magnetic Helicity Conservation and Inverse Energy Cascade in Electron Magnetohydrodynamic Wave Packets. *Phys. Rev. Lett.* **2011**, *106*, 191104.
133. Ji, H. Turbulent dynamos and magnetic helicity. *Phys. Rev. Lett.* **1999**, *83*, 3198–3201.
134. Galtier, S.; Bhattacharjee, A. Anisotropic weak whistler wave turbulence in electron magnetohydrodynamics. *Phys. Plasmas* **2003**, *10*, 3065–3076.
135. Kim, H.; Cho, J. Inverse cascade in imbalanced electron magnetohydrodynamic turbulence. *Astrophys. J. Suppl.* **2015**, *801*, 75.